PLOS BIOLOGY

RESEARCH ARTICLE

Selective suppression of oligodendrocyte-derived amyloid beta rescues neuronal dysfunction in Alzheimer's disease

Rikesh M. Rajani[1]*, Robert Ellingford[1], Mariam Hellmuth[1], Samuel S. Harris[1], Orjona S. Taso[1], David Graykowski[1], Francesca Kar Wey Lam[1], Charles Arber[2], Emre Fertan[3,4], John S. H. Danial[3,4,5], Matthew Swire[6], Marcus Lloyd[6], Tatiana A. Giovannucci[2], Mathieu Bourdenx[1], David Klenerman[3,4], Robert Vassar[7], Selina Wray[2], Carlo Sala Frigerio[1], Marc Aurel Busche[1]*

1 UK Dementia Research Institute at UCL, University College London, London, United Kingdom, **2** Department of Neurodegenerative Disease, University College London Queen Square Institute of Neurology, London, United Kingdom, **3** Yusuf Hamied Department of Chemistry, University of Cambridge, Cambridge, United Kingdom, **4** UK Dementia Research Institute at University of Cambridge, Cambridge, United Kingdom, **5** School of Physics and Astronomy, University of St Andrews, St. Andrews, United Kingdom, **6** Wolfson Institute for Biomedical Research, University College London, London, United Kingdom, **7** Department of Neurology, Feinberg School of Medicine, Northwestern University, Chicago, Illinois, United States of America

* r.rajani@ucl.ac.uk (RMR); m.busche@ucl.ac.uk (MAB)

OPEN ACCESS

Citation: Rajani RM, Ellingford R, Hellmuth M, Harris SS, Taso OS, Graykowski D, et al. (2024) Selective suppression of oligodendrocyte-derived amyloid beta rescues neuronal dysfunction in Alzheimer's disease. PLoS Biol 22(7): e3002727. https://doi.org/10.1371/journal.pbio.3002727

Academic Editor: Mikael Simons, Max-Planck-Institut fur experimentelle Medizin, GERMANY

Received: June 27, 2024

Accepted: July 1, 2024

Published: July 23, 2024

Peer Review History: PLOS recognizes the benefits of transparency in the peer review process; therefore, we enable the publication of all of the content of peer review and author responses alongside final, published articles. The editorial history of this article is available here: https://doi.org/10.1371/journal.pbio.3002727

Data Availability Statement: The full dataset is available from the corresponding authors upon reasonable request and will be stored on UCL Research Data Repository. All data necessary to

Abstract

Reduction of amyloid beta (Aβ) has been shown to be effective in treating Alzheimer's disease (AD), but the underlying assumption that neurons are the main source of pathogenic Aβ is untested. Here, we challenge this prevailing belief by demonstrating that oligodendrocytes are an important source of Aβ in the human brain and play a key role in promoting abnormal neuronal hyperactivity in an AD knock-in mouse model. We show that selectively suppressing oligodendrocyte Aβ production improves AD brain pathology and restores neuronal function in the mouse model in vivo. Our findings suggest that targeting oligodendrocyte Aβ production could be a promising therapeutic strategy for treating AD.

Introduction

Alzheimer's disease (AD) is a devastating neurodegenerative disorder affecting millions of people worldwide. Accumulation of amyloid beta (Aβ) is an early critical hallmark of the disease and thus is an important target for understanding pathophysiology and therapy. Recent clinical trials demonstrating a slowing of cognitive and functional decline in individuals with AD treated with anti-Aβ antibodies indeed reinforce the important role of Aβ in AD pathophysiology [1,2]. Among the earliest responses of neurons to this accumulation of Aβ is an abnormal increase in excitability [3,4]. However, neurons are not the only cells to react to Aβ. Recently, transcriptomic studies have shown changes not only in microglia and astrocytes but also in oligodendrocytes, the myelinating cells of the central nervous system, in both human AD tissue [5,6] and in mouse models of AD [7,8]. In addition, genetic risk associated with AD

reproduce all figures is available within the Source data provided with this paper. Example MATLAB (MathWorks) scripts used for examining pre-processed electrophysiological data are available at: https://doi.org/10.5281/zenodo.12627166.

Funding: R.M.R, D.K., C.S.F. and M.A.B. are supported by the UK Dementia Research Institute through UK DRI Ltd, principally funded by the UK Medical Research Council. M.A.B. is further supported by an UKRI Future Leaders Fellowship (MR/X011038/1) and an NC3Rs studentship grant (NC/W001675/1). S.S.H. is supported by an Alzheimer's Association International Research Fellowship (AARF-23-1149637). C.A. and S.W. are supported by the National Institute for Health and Care Research University College London Hospitals Biomedical Research Centre. M.S. is supported by an MRC Career Development Award (MR/X019977/1). T.A.G. is supported by an Alzheimer's Association Research Fellowship to Promote Diversity (23AARFD-1029918). The funders had no role in study design, data collection and analysis, decision to publish, or preparation of the manuscript. Funding websites: UK DRI - http://ukdri.ac.uk UKRI/Medical Research Council - https://www.ukri.org/councils/mrc/ NC3Rs - https://www.nc3rs.org.uk NIHR - https://www.uclhospitals.brc.nihr.ac.uk Alzheimer's Association - https://www.alz.org.

Competing interests: C.S.F. is currently employed by GSK. The other authors have declared that no competing interests exist.

Abbreviations: AD, Alzheimer's disease; ARIA, amyloid-related imaging abnormalities; CV, coefficient of variation; CCF, Common Coordinate Framework; FOV, field of view; GIM, glial induction medium; GMM, Gaussian mixture distribution model; DM, differentiation media; fAD, familial AD; ICC, immunocytochemistry; IHC, immunohistochemistry; iPSC, induced pluripotent stem cell; ISH, in situ hybridization; ISI, inter-spike interval; LFP, local field potential; MACS, Magnetic-Activated Cell Sorting; MFR, mean firing rate; MOI, multiplicity of infection; NPC, neural precursor cell; OCT, optimal cutting temperature compound; OPC, oligodendrocyte precursor cell; PBS, phosphate-buffered saline; PEG, polyethylene glycol; PETH, peri-event time histogram; PFA, paraformaldehyde; RPM, rotations per minute; RT, room temperature; sAD, sporadic AD; snRNA-seq, single nucleus RNA sequencing; SWR, sharp wave ripple; UCL, University College London; WT, wild type.

is enriched in age-dependent transcriptome networks of both microglia and oligodendrocytes [9].

Despite these key cellular effects of Aβ, and its essential role in AD, the traditional assumption that neurons are the primary source of pathogenic Aβ in the brain has remained untested. In this study, we show that oligodendrocytes in human tissue contain all of the components required to produce Aβ, and that human oligodendrocytes produce soluble Aβ in vitro. We further show that selectively suppressing oligodendrocyte Aβ production in an AD mouse model is sufficient to rescue abnormal neuronal hyperactivity. Thus, we provide evidence for a critical role of oligodendrocyte-derived Aβ for early neuronal dysfunction in AD.

Results

Oligodendrocytes contain all components required to produce Aβ

To identify the cell types in the brain that are intrinsically capable of producing Aβ, we exploited four publicly available human single nucleus RNA sequencing (snRNA-seq) datasets [5,10–12] and examined expression levels of genes involved in the production of Aβ: the amyloid precursor protein (*APP*), beta secretase (*BACE1*), and components of gamma secretase [presenilin (*PSEN*) 1, *PSEN2*, nicastrin (*NCSTN*), *APH1A*, *APH1B*, *PSENEN*]. We found that, apart from *PSEN2* (which is not essential for gamma secretase function when *PSEN1* is present [13]), oligodendrocytes had elevated expression of all of these genes (**Fig 1A–1D**). Remarkably, many genes were expressed at a higher level in oligodendrocytes than in any other cell type in the brain, including notably neurons (**Fig 1A–1D**). With the exception of neurons and oligodendrocytes, no other cell type examined was found to highly express all of the genes required for Aβ production (**Fig 1A–1D**), suggesting that oligodendrocytes, uniquely among glia, have an intrinsic capacity to produce Aβ. To confirm that this is not limited to RNA, we exploited publicly available proteomics data derived from isolated mouse brain cells [14] and found that, at the protein level, oligodendrocytes indeed contain high levels of APP, BACE1, and PSEN1 (**S1 Fig**). We further confirmed the presence of APP and BACE1 protein in mouse oligodendrocytes by immunohistochemistry (**Figs 1E, 1F, and S2**).

Human AD brains possess more oligodendrocytes with the capacity to produce Aβ

To validate these findings, and to determine whether the capacity of oligodendrocytes to produce Aβ is altered in AD, we performed RNAscope in situ hybridization (ISH) on postmortem tissue from the brains of patients with sporadic AD (sAD) and controls for *MBP* (a gene expressed exclusively in oligodendrocytes in the central nervous system [15]), *APP*, and *BACE1* (**Fig 2A**). We found that approximately 80% of oligodendrocytes express both *APP* and *BACE1* in Layers 5/6 of both sAD patient and control brains, indicating that they are capable of producing Aβ (**Fig 2B**). Contrary to our expectation of oligodendrocyte loss associated with myelin loss in AD [16], we observed an increased number of oligodendrocytes in Layers 5/6 of the prefrontal cortex of brains from sAD patients (**Fig 2C**), which was not solely explained by age (**S3A Fig**) and was not seen in Layers 2/3 of the prefrontal cortex (**S3B Fig**). Combined with the equivalent proportion of oligodendrocytes expressing both *APP* and *BACE1*, this increase in oligodendrocyte density resulted in an increased number of Aβ-capable oligodendrocytes within the brains of sAD patients (**Fig 2D**). By examining all cells expressing both *APP* and *BACE1*, we observed an increase in the total number of APP^+ $BACE1^+$ cells in the brains of sAD patients (**S3C Fig**), which was driven by an elevated proportion of APP^+ $BACE1^+$ cells that are oligodendrocytes (**S3D Fig**). Notably, there was no change

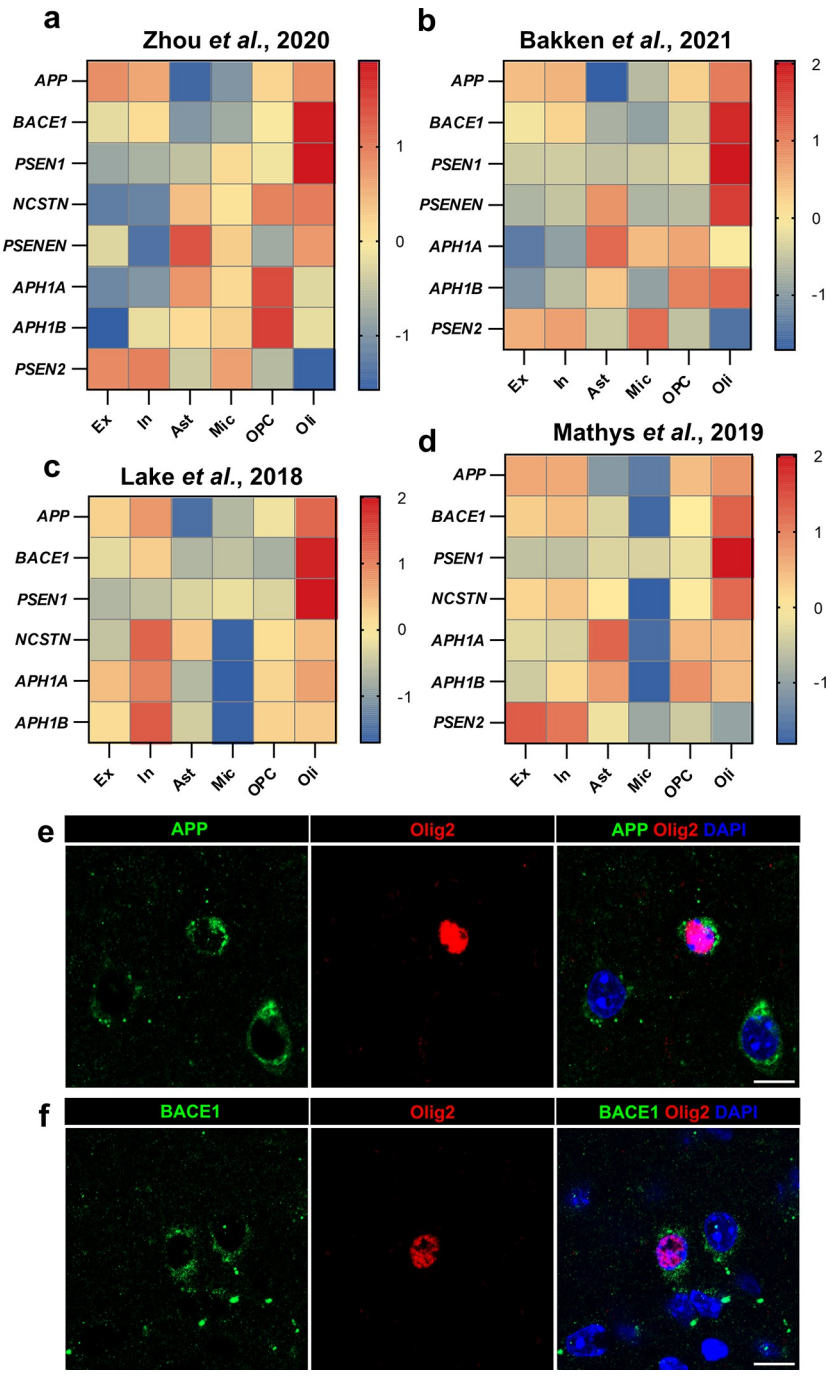

Fig 1. Components required to produce Aβ are expressed at high levels in oligodendrocytes, but not other glial cells. Heatmaps showing the $\log_2$ (norm count) z-score of genes of interest across different cell types [Excitatory neurons (Ex), Inhibitory neurons (In), Astrocytes (Ast), Microglia (Mic), Oligodendrocyte Precursor Cells (OPC), and Oligodendrocytes (Oli)], from 4 publicly available human single nucleus RNA sequencing datasets. *APP*, *BACE1*, and all components of γ-secretase (*PSEN1*, *PSENEN*, *NCSTN*, *APH1A*, *APH1B*) with the exception of *PSEN2* (which is interchangeable with *PSEN1*) are expressed at high levels in oligodendrocytes, many at higher levels than any other cell type. (**a**) Data from Zhou and colleagues [10] was generated using tissue from the motor cortex of 36 subjects including controls, AD patients, and those carrying TREM2 variants. (**b**) Data from Bakken and colleagues [11] was generated using tissue from the motor cortex of 5 control subjects. (**c**) Data from Lake and colleagues [12] was generated using tissue from the frontal cortex of 6 control subjects. (**d**) Data from Mathys and colleagues [5] was generated using tissue from the prefrontal cortex of 48 subjects with varying degrees of AD-related pathology. (**e**) Representative immunofluorescent images showing APP (green), oligodendroglial marker Olig2 (red), and DAPI (nuclei; blue) in the

cortex of a 4-month-old wild-type mouse. Scale bar = 10 μm. (**f**) Representative immunofluorescent images showing BACE1 (green), oligodendroglial marker Olig2 (red), and DAPI (nuclei; blue) in the cortex of a 4-month-old wild-type mouse. Scale bar = 10 μm.

https://doi.org/10.1371/journal.pbio.3002727.g001

in the number of other cells (*MBP*$^{-}$) capable of producing Aβ (S3E Fig), which were almost exclusively neurons (labelled as *RBFOX3*$^{+}$, a gene expressed in all neurons in the cortex; S3F–S3I Fig).

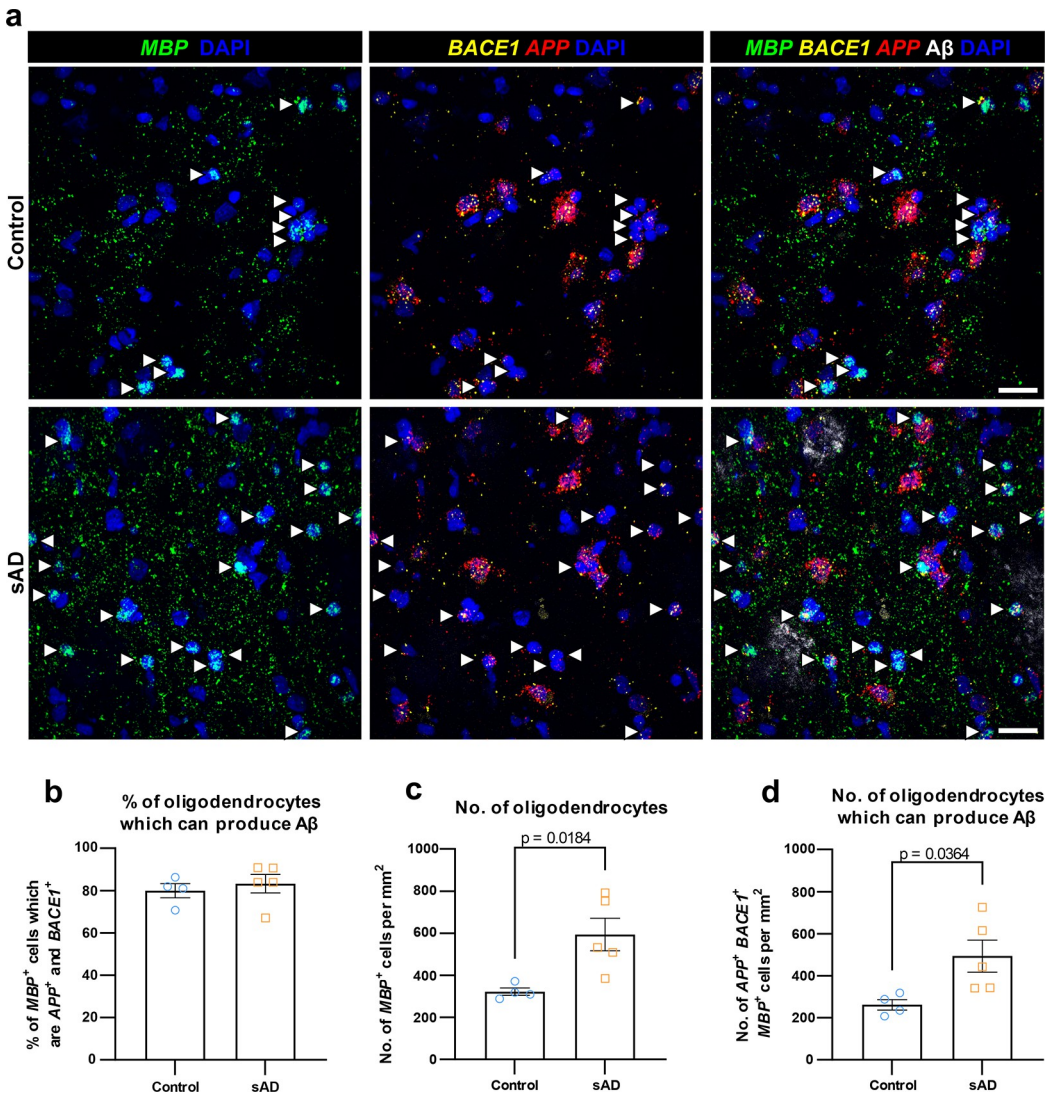

Fig 2. Human sporadic AD brains have more oligodendrocytes capable of producing Aβ compared to controls. (**a**) Fluorescence images from Layers 5/6 of control (top) and sporadic AD (sAD; bottom) postmortem human prefrontal cortex labelled for *MBP* (oligodendrocyte-specific gene; green), *BACE1* (yellow), *APP* (red), Aβ (identified by 6E10-antibody; white), and DAPI (nuclei; blue). Aβ-capable oligodendrocytes (*MBP*$^{+}$ *BACE1*$^{+}$ *APP*$^{+}$ nuclei) are marked with white arrowheads. Scale bar = 25 μm. (**b**) Quantification showing that approximately 80% of oligodendrocytes are capable of producing Aβ in both control and sAD brains. (**c**) Quantification showing an increase in the number of oligodendrocytes in Layers 5/6 of sAD brains. (**d**) Quantification showing significantly more Aβ-capable oligodendrocytes in sAD brains than controls. In (**b**–**d**), each data point represents a single brain ($n = 4$ control brains, $n = 5$ sAD brains) with bars representing mean ± SEM; unpaired t test: $t(7) = 0.568, 3.058, 2.581$ in (**b**–**d**), respectively. Source data are available in S1 Data.

https://doi.org/10.1371/journal.pbio.3002727.g002

We additionally carried out densitometric analysis of *APP* and *BACE1* spots within oligodendrocytes and neurons. On average, oligodendrocytes were found to express higher amounts of *APP* and *BACE1* than neurons (**S4A and S4B Fig**), though neurons showed a greater variability in expression levels, with a subset of neurons showing very high expression yet others showing only minimal expression (**S4C and S4D Fig**). The observed increase in the number of Aβ-capable oligodendrocytes in sAD brains suggests that oligodendrocyte Aβ production may play an important, but hitherto unappreciated, role in the pathogenesis of the disease.

Human iPSC-derived oligodendrocytes produce Aβ

As well as expressing the components necessary for Aβ production, it is pathologically relevant to understand whether human oligodendrocytes do indeed produce Aβ. To determine this, we differentiated oligodendrocytes from human induced pluripotent stem cells (iPSCs) following a previously established protocol [17]. We used iPSCs derived from familial AD (fAD) patients as well as an isogenic control, to examine this question in well-established lines both with and without pathological mutations affecting Aβ production [18,19]; due to the rarity of iPSC lines with fAD mutations, we did not compare between different lines, but considered them together. After 30 days of maturation, these cultures contained 6.3% MBP^+ oligodendrocytes and 87.3% oligodendrocyte precursor cells (OPCs)/pre-myelinating oligodendrocytes, but almost no other non-oligodendroglial cell types (**Figs 3A and S5A–S5C**), consistent with previous studies [17]. Across all lines tested, we found that human iPSC-derived oligodendrocytes indeed produced Aβ, and that this Aβ production was significantly reduced by administration of the BACE1 inhibitor NB-360 [20], indicating that Aβ production in oligodendrocytes is BACE1 dependent (**Fig 3B**). Notably, this reduction in Aβ production is similar to what has previously been shown in human iPSC-derived neurons upon administration of NB-360 or similar BACE inhibitors [21–24]; these data from human iPSCs are also consistent with, and translationally extend, previous findings from rat and human embryonic stem cell oligodendrocyte cultures [25,26].

Next, to understand how oligodendrocyte Aβ production compares to neuronal Aβ production, we generated human iPSC-derived cortical neurons from the same cell lines following a previously established protocol [27] (**S5D–S5G Fig**), and normalised the amount of Aβ produced to cell number. Under the experimental conditions tested, we found that oligodendrocytes produce more Aβ than neurons derived from the same cell line, both in lines from fAD patients with PSEN1 mutations and an isogenic control (**Fig 3C**). We additionally quantified Aβ production by human iPSC-derived OPCs, microglia and astrocytes (**S7A–S7F Fig**) and found that these cells produce only low amounts of Aβ (**S7G Fig**), consistent with our analyses of snRNA-seq data (**Fig 1A–1D**).

We next compared the Aβ species produced between the cell types and found that oligodendrocytes had an increased Aβ 42:40 ratio relative to neurons from the same line (**Fig 3D**). This observation suggests that oligodendrocytes could potentially generate a relatively higher proportion of longer Aβ species, which are more prone to aggregation [28] and, consequently, could be more pathogenic than shorter Aβ species. We therefore used a single-molecule pull-down (SiMPull) assay with DNA-PAINT super-resolution imaging [29] to analyse soluble Aβ aggregates, of a size consistent with oligomers and protofibrils, in the media from these cells (**Figs 3E, S8A, and S8B**). This technique relies on dual binding of a single epitope antibody and clustering analysis requiring close proximity of at least 2 of these super-resolved assemblies to ensure specific detection of soluble aggregates, and has previously been validated to detect stable soluble aggregates with a high sensitivity [29–31] (see Methods for details).

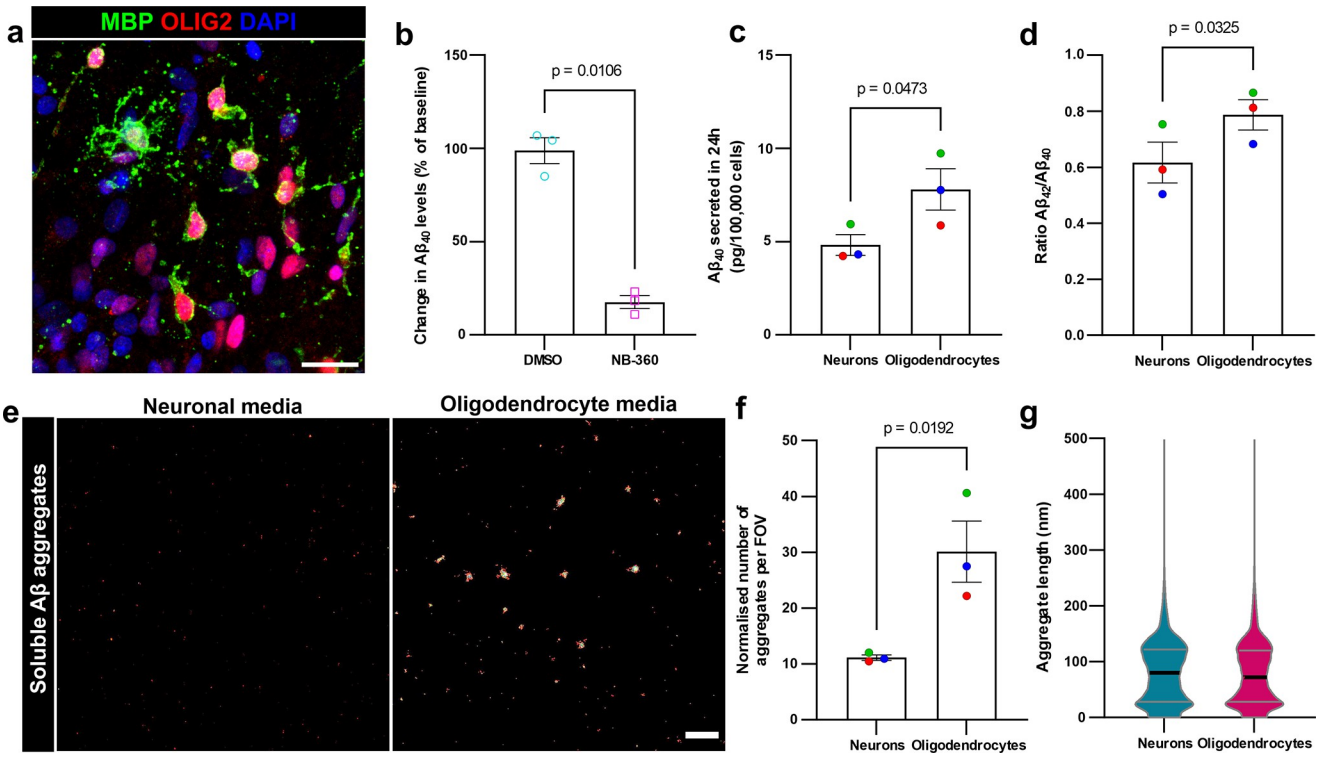

Fig 3. Human oligodendrocytes produce soluble Aβ and aggregates at higher levels than neurons. (**a**) Fluorescent image of human iPSC-derived oligodendrocyte culture immunolabelled for MBP (green), OLIG2 (marker of all oligodendroglia; red), and DAPI (nuclei; blue). This example shows multiple mature oligodendrocytes extending MBP^+ myelin processes, while the majority of other cells are $OLIG2^+$ MBP^- OPCs. Scale bar = 25 μm. (**b**) Quantification by ELISA showing a significant reduction in the amount of $A\beta_{40}$ produced (as a % of the amount produced prior to treatment) by human oligodendrocytes when treated with BACE1 inhibitor (NB-360) compared to vehicle control (DMSO). (**c**) ELISA data showing more $A\beta_{40}$ produced by oligodendrocytes than neurons derived from the same fAD human-iPSC lines. (**d**) Quantification by ELISA showing higher $A\beta_{42}/A\beta_{40}$ ratio produced by oligodendrocytes compared to neurons derived from the same fAD human-iPSC lines. (**e**) DNA-PAINT super-resolution images showing more Aβ aggregates in media from oligodendrocytes (right) compared to neurons (left). Scale bar = 1 μm. (**f**) Quantification showing oligodendrocytes produce a higher proportion of Aβ as aggregates compared to neurons derived from the same fAD human-iPSC lines. (**g**) Violin plots showing the length of aggregates produced by neurons and oligodendrocytes (mean ± standard deviation: Neurons 79.8 nm ± 58.7 nm, Oligodendrocytes 77.7 nm ± 58.5 nm; n = 18,550 aggregates from 3 neuron lines [3 independent inductions per line] and 24,719 aggregates from 3 oligodendrocyte lines [3 independent inductions per line]). In (**b**), each data point represents the average of 2 independent inductions from each of a different cell line (n = 3 cell lines), with bars showing mean ± SEM; paired t test: $t(2) = 9.613$. In (**c, d, f**), each data point represents the average of 4 (for PSEN1 WT line neurons in **d**) or 3 independent inductions from each of a different cell line (n = 3 cell lines), showing mean ± SEM with each cell line shown in a different colour to highlight pairing (blue: PSEN1 WT; green: PSEN1 int4del; red: PSEN1 R278I); paired t test: $t(2) = 4.435, 5.411$ in (**c, d**), respectively; ratio paired t test: $t(2) = 7.117$ in (**f**). Unpooled data for (**b, c, d, f**) are shown in S6 Fig. Source data are available in S1 Data. fAD, familial AD; iPSC, induced pluripotent stem cell; MBP, myelin basic protein; OPC, oligodendrocyte precursor cell.

https://doi.org/10.1371/journal.pbio.3002727.g003

Intriguingly, our analysis revealed that oligodendrocytes produced a greater quantity of these soluble Aβ aggregates than neurons, exceeding the levels that would be anticipated based on the increased amount of Aβ produced (Fig 3E and 3F). Furthermore, we found that the majority of aggregates produced by both oligodendrocytes and neurons were between 20 nm and 200 nm in length (**Figs** 3G and S8C), consistent with the reported size of synaptotoxic Aβ aggregates from human AD brains [32]. These results suggest that Aβ produced by oligodendrocytes has a higher propensity for aggregation than neuron-derived Aβ.

Oligodendrocyte-derived Aβ contributes to plaque formation in vivo

To directly investigate whether these features of oligodendrocyte-produced Aβ are consequential for Aβ plaque formation in vivo, we generated $App^{NL\text{-}G\text{-}F}$ knock-in mice [33] with BACE1 knocked out specifically in either oligodendrocytes ($BACE1^{fl/fl}$;PLP1-Cre/$ERT^{+/-}$;$App^{NL\text{-}G\text{-}F}$)

or neurons (BACE1$^{fl/fl}$;Thy1-Cre/ERT2,-EYFP$^{+/-}$;*App*$^{NL-G-F}$). We elected to use the *App*$^{NL-G-F}$ knock-in mouse model for this study as it expresses *App* under its endogenous promoter in a physiological manner with regards to both cell type and amount, and avoids the issue of APP overexpression and abnormal expression patterns. To avoid developmental and early postnatal effects of BACE1 knockout on myelin [34], we used tamoxifen inducible Cre lines, with tamoxifen administered between the ages of 4 and 8 weeks (after the majority of developmental myelination has taken place [35]), according to standard protocols [36]. Indeed, several control experiments confirmed that this approach had no significant effect on the amount of MBP (**S9A and S9B Fig**), myelin sheath lengths (**S9C and S9D Fig**), the number of oligodendrocytes (**S10A–S10C Fig**), or oligodendrocyte autophagy (**S11A–S11F Fig**).

We assessed Aβ plaque load within the visual, retrosplenial, and motor cortex of these mice at 4 months of age, when there is already widespread plaque distribution within the cortex of *App*$^{NL-G-F}$ mice [33]. We found that oligodendrocyte-specific knockout of BACE1 led to approximately 25% reduction in the number of plaques across the combined area of these cortical regions compared to unmodified *App*$^{NL-G-F}$ control mice (**Fig 4A and 4B**), while knockout of BACE1 specifically in neurons led to a near elimination of plaques within the cortex (**Fig 4A–4C**). Notably, oligodendrocyte-specific knockout of BACE1 led to a greater reduction in plaque area in cortical Layers 5/6 as compared to Layers 2/3 specifically within the retrosplenial cortex, which is known to be a selectively vulnerable site of early plaque deposition and functional impairment in AD [37] (**S12A and S12E Fig**), albeit not within the motor cortex (**S12B and S12F Fig**). A similar trend in 20% to 30% plaque reduction was also observed in the CA1 area of the hippocampus and the corpus callosum, a major white matter tract (**S12C, S12D, S12G, and S12H Fig**). These results are consistent with our analysis of snRNA-seq data, where oligodendrocytes had high expression of genes required to produce Aβ in all of the datasets from different brain regions (**Fig 1A–1D**).

Suppression of oligodendrocyte-derived Aβ rescues neuronal dysfunction in *App*$^{NL-G-F}$ mice in vivo

To determine the consequences of BACE1 knockout in oligodendrocytes on neuronal dysfunction in vivo, we used high-density Neuropixels probes to record ongoing neuronal action potential firing in the retrosplenial cortex of 3-month-old awake mice. We found that that oligodendrocyte-specific knockout of BACE1 abolished the early abnormal neuronal hyperactivity phenotype that is present in the *App*$^{NL-G-F}$ mice, which has been shown to be dependent on soluble Aβ [38–40] (**Fig 5A and 5B**). Notably, in *App*$^{NL-G-F}$ mice with an oligodendrocyte-specific knockout of BACE1, we observed that not only were the levels of neuronal firing restored to those seen in WT controls, but so too also the temporal structure, as indicated by the analysis of the variability in mean firing rates (MFRs) and inter-spike intervals (**S13 Fig**). We also analysed the power spectrum of cortical local field potentials (LFPs) in the BACE1 knockout mice but found no significant changes compared to controls (**S14 Fig**). In addition, analyses of multiunit neuronal responses in retrosplenial cortex to sharp-wave ripple (SWR) events in CA1 during awake rest [41] did not reveal any notable impairments in the timing or magnitude of cortical neuronal responses in the BACE1 knockout animals compared to controls (**S15 Fig**). Together, these findings indicate that BACE1 knockout in oligodendrocytes effectively ameliorates abnormal neuronal hyperactivity in *App*$^{NL-G-F}$ mice without disrupting the electrophysiological integrity of the cortical-hippocampal network.

Our results that targeted suppression of Aβ production in oligodendrocytes can rescue neuronal hyperactivity, even without the complete elimination of plaques, indicated that soluble Aβ species produced by oligodendrocytes may in fact contribute to early neuronal dysfunction

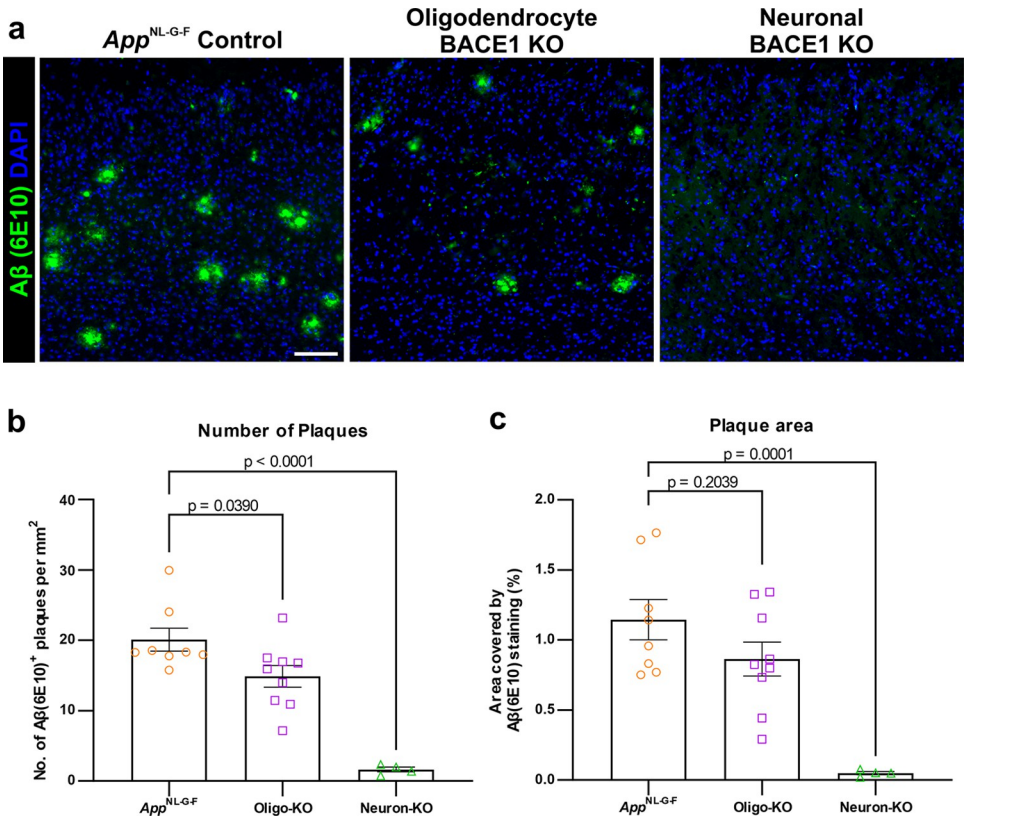

Fig 4. Genetic suppression of oligodendrocyte Aβ production reduces Aβ plaques in the *App*$^{NL-G-F}$ mouse model of AD. (a) Immunofluorescent images showing Aβ (6E10 antibody; green) and DAPI in the retrosplenial cortex of *App*$^{NL-G-F}$ control mice (left), *App*$^{NL-G-F}$ mice with BACE1 knocked out (KO) specifically in oligodendrocytes (middle; Oligo-KO), and *App*$^{NL-G-F}$ mice with BACE1 KO specifically in neurons (right; Neuron-KO). Images show all layers of the cortex, with Layer 6 at the bottom. Scale bar = 100 μm. **(b)** Quantification of the number of Aβ^{+} plaques across the visual, retrosplenial, and motor cortical areas, showing a 25% reduction in Oligo-KO mice compared to *App*$^{NL-G-F}$, and an elimination of plaques in Neuron-KO mice. **(c)** Quantification of the total area of Aβ^{+} plaques across the visual, retrosplenial, and somatomotor cortical areas, showing approximately 25% reduction in Oligo-KO mice compared to *App*$^{NL-G-F}$ and an elimination of plaques in Neuron-KO mice. In (**b and c**), data points represent individual mice (n = 8 *App*$^{NL-G-F}$, 9 Oligo-KO, 4 Neuron-KO) with bars showing mean ± SEM. One-way ANOVA with Dunnet's post hoc tests: $F(2,18) = 25.38$(**b**), 13.24(**c**); $p < 0.0001$(**b**), $p = 0.0003$(**c**). Source data are available in S1 Data.

https://doi.org/10.1371/journal.pbio.3002727.g004

in the AD brain. To directly test this hypothesis, we injected human fAD iPSC-derived oligodendrocyte conditioned media containing soluble Aβ aggregates into the retrosplenial cortex of WT mice while recording ongoing neuronal action potential firing using Neuropixels in vivo. As controls, we administered the same media immunodepleted of Aβ using 6E10 antibody, or media from oligodendrocytes which had been treated with BACE1 inhibitor in order to suppress Aβ production. Indeed, we found that neuronal firing rates were markedly increased during injection of the oligodendrocyte conditioned media compared to baseline, which was not observed with control media (Fig 5C and 5D). These results suggest that oligodendrocyte-derived Aβ is sufficient to promote neuronal hyperactivity, in the absence of Aβ from any other cellular source.

Discussion

In conclusion, we have shown that human oligodendrocytes not only produce Aβ, but they can also generate Aβ in greater amounts and with a higher proportion as soluble aggregates

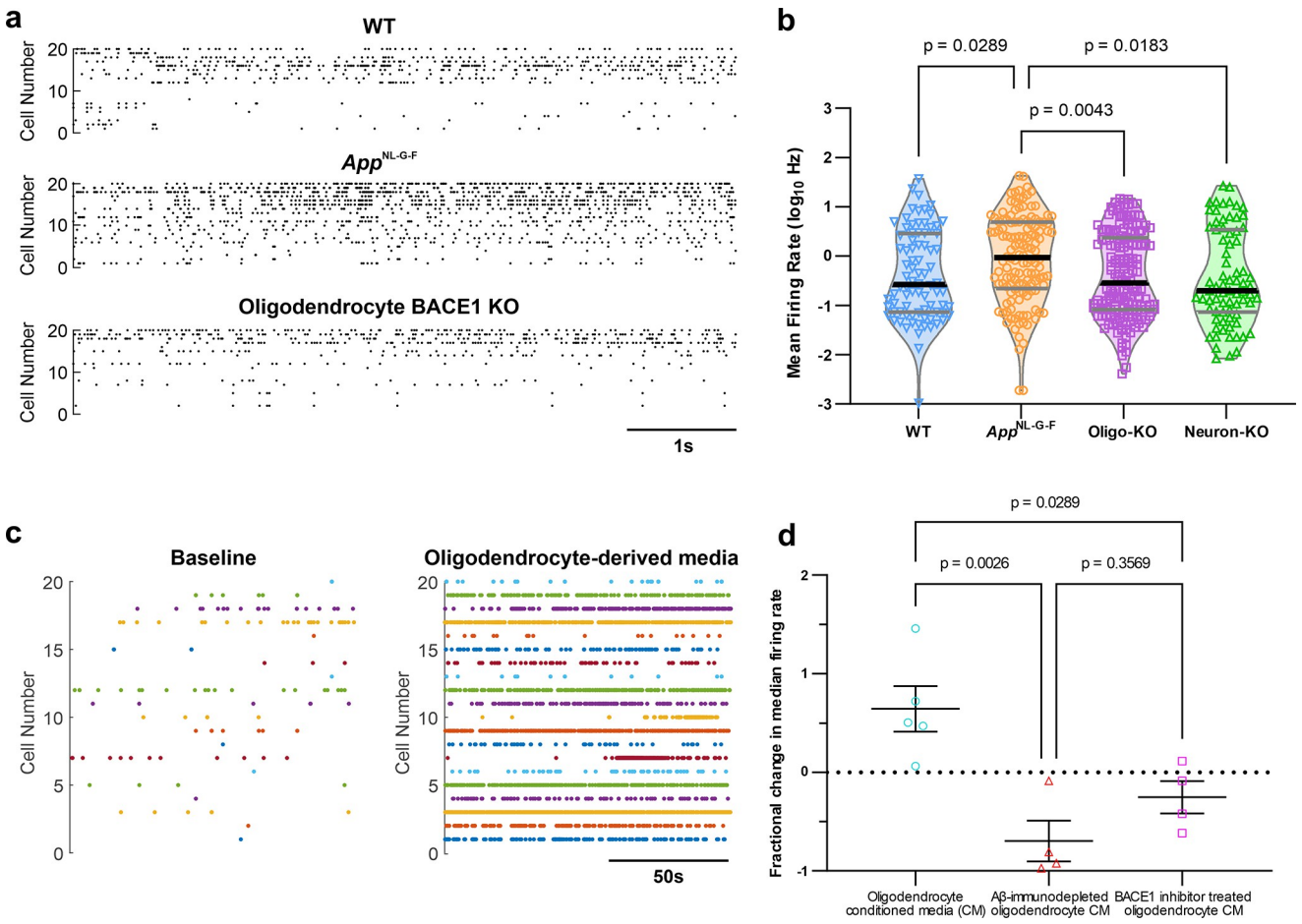

Fig 5. Genetic suppression of oligodendrocyte Aβ production rescues neuronal dysfunction in the *App*$^{NL-G-F}$ mouse model of AD, while oligodendrocyte-derived media promotes neuronal dysfunction in vivo. **(a)** Raster plots from Neuropixels recordings showing spontaneous neuronal firing in 20 randomly selected cortical neurons/units from 3-month-old awake WT (top), *App*$^{NL-G-F}$ (middle) and oligodendrocyte BACE1 KO (bottom) mice, illustrating rescue of hyperactivity phenotype in oligodendrocyte BACE1 KO mice to WT levels. Units are sorted from high MFRs to low (top to bottom) and plots show a 6s resting state period. (**b**) Quantification of the MFR showing significantly reduced activity in cortical neurons of both Oligo-KO and Neuron-KO mice compared to *App*$^{NL-G-F}$ mice, with firing rates returning to levels observed in WT controls (WT vs. Oligo-KO: $p > 0.9999$; WT vs. Neuron-KO: $p > 0.9999$). In **(b),** data points represent individual neurons/units ($n = 82$ WT, 134 *App*$^{NL-G-F}$, 165 Oligo-KO, 75 Neuron-KO) across 4 (WT) or 3 mice per group with the shaded area representing smoothed distribution. Median is shown by a thick black line, and quartiles indicated with grey lines. Kruskal–Wallis test ($H(3, n = 456) = 15.33$, $p = 0.0016$) with Dunn's post hoc tests. (**c**) Raster plots showing neuronal firing in the same 20 cortical neurons/units at baseline (left) and during injection of oligodendrocyte conditioned media containing soluble Aβ aggregates (right) in a 4-month-old WT mouse, illustrating the strong increase in neuronal activity upon exposure to oligodendrocyte-derived Aβ. **(d)** Quantification showing an increase in neuronal firing rates upon local injection of oligodendrocyte conditioned media ($Aβ_{40}$ concentration by ELISA: 133 pM) into retrosplenial cortex, compared to injection of either the same media which had been immunodepleted of Aβ ($Aβ_{40}$ concentration by ELISA: 24 pM) or media from BACE1 inhibitor-treated oligodendrocytes ($Aβ_{40}$ concentration by ELISA: 18 pM). In (**d**), data points represent individual mice ($n = 5$ oligodendrocyte conditioned media, 4 other groups) with mean ± SEM shown. One-way ANOVA ($F(2,10) = 11.23$, $p = 0.0028$) with Tukey's post hoc tests. Source data are available in S1 Data. AD, Alzheimer's disease; KO, knockout; MFR, mean firing rate.

https://doi.org/10.1371/journal.pbio.3002727.g005

compared to neurons. This was seen in oligodendrocytes both with and without fAD mutations. The increased Aβ 42:40 ratio in oligodendrocytes could contribute to the high proportion of soluble aggregates [28,42,43]; it is also worth noting that the relationship between Aβ monomer concentration and aggregate concentration is nonlinear, so small changes in monomer can result in larger increases in the number of aggregates [44], although this does not rule out additional contributing factors. We demonstrate that specific suppression of oligodendrocyte Aβ production is sufficient to rescue neuronal hyperactivity in the *App*$^{NL-G-F}$ knock-in model of AD. In turn, administration of oligodendrocyte conditioned media containing

soluble Aβ promotes neuronal hyperactivity in WT mice in vivo. This result is consistent with, and extends, previous studies on the effects of soluble Aβ on neuronal activity, although these earlier studies did not consider the cellular source of Aβ [38–40].

The functional rescue is remarkable given the relatively modest reduction in plaque load that results from blocking oligodendrocyte Aβ production, while blocking neuronal Aβ production leads to a near elimination of plaques. This aligns with work from multiple laboratories showing that plaque formation depends on neuronal Aβ [45–48] and is consistent with the lower abundance of plaques observed in the white matter compared to the grey matter, although elevated levels of soluble Aβ have previously been reported in the white matter of individuals with AD [49]. The lower abundance of plaques in the white matter could further be explained by the evidence that most neuronal Aβ is secreted at presynaptic terminals, thus favouring plaque deposition in the grey matter [50,51]. This small contribution of oligodendrocytes to plaque load could suggest that a main effect of oligodendrocyte-derived Aβ is to promote neuronal dysfunction. Rather than being plaque dependent, the effects of Aβ on neuronal activity and synaptic function often stem from soluble aggregates similar to those we see produced in much greater numbers by oligodendrocytes [32,39].

Together with our data showing an increased number of Aβ-producing oligodendrocytes in deeper cortical layers of the brains of individuals with AD, these results indicate that oligodendrocyte-derived Aβ plays a pivotal role in the early impairment of neuronal circuits in AD [52], which has important implications for how we consider and treat the disease. The increased number of oligodendrocytes in human AD brains also raises the intriguing possibility that these cells could potentially offset reduced Aβ production due to neuronal loss as the disease progresses. While recent anti-Aβ antibody therapies targeting plaques have been shown to be effective in slowing the clinical course of AD, they can lead to blood vessel damage, detected as amyloid-related imaging abnormalities (ARIA) on MRI [53]. Previous trials to reduce Aβ through BACE inhibition have failed to demonstrate similar beneficial effects, which is thought to be due to the effects on other neuronal BACE substrates such as SEZ6 [54], which, importantly, is not expressed in oligodendrocytes (**S16 Fig**). Thus, to circumvent such unwanted effects, we propose that blocking Aβ production specifically in oligodendrocytes, for example, by employing oligodendrocyte-targeting AAVs [55], may constitute a promising novel target for treating AD.

Materials and methods

Animals

All experimental procedures were conducted in accordance with the Animal (Scientific procedures) Act 1986, approved by the Animal Welfare and Ethical Review Body at University College London (UCL), and performed under an approved UK Home Office project licence at UCL (PP8718352 to MAB). Mice were maintained in a 12-h light/dark cycle with food and water supplied ad libitum. *App*$^{NL\text{-}G\text{-}F}$ mice [C57BL/6-App<tm3(NL-G-F)Tcs> (No. RBRC06344)] were provided by the RIKEN BRC through the National BioResource Project of the MEXT, Japan [33]. BACE1$^{fl/fl}$ mice (C57BL/6-Bace1tm1.1mrl) were previously generated and provided by R.V. [36]. PLP1-Cre/ERT mice [B6.Cg-Tg(Plp1-cre/ERT)3Pop/J; JAX:005975] and Thy1-Cre/ERT2,-EYFP mice [B6.Tg(Thy1-cre/ERT2,-EYFP)HGfng/PyngJ; JAX:012708] were purchased from The Jackson Laboratory. Three mouse cohorts were generated: (1) BACE1$^{fl/fl}$;PLP-Cre/ERT$^{+/-}$;*App*$^{NL\text{-}G\text{-}F}$; (2) BACE1$^{fl/fl}$;Thy1-Cre/ERT,-EYFP$^{+/-}$; *App*$^{NL\text{-}G\text{-}F}$; and (3) BACE1$^{fl/fl}$;*App*$^{NL\text{-}G\text{-}F}$ (i.e., the Cre/ERT$^{-/-}$ littermates from the other 2 cohorts). All 3 cohorts were treated with tamoxifen between 4 and 8 weeks of age: tamoxifen (MP Biomedicals; 156738) was dissolved in corn oil at 25 mg/ml. Animals were injected with

tamoxifen intraperitoneally at a dose of 100 mg/kg daily for 5 days followed by a 2 day break, repeated 4 times. For Neuropixels recordings, C57BL/6J mice (originally purchased from Charles River Laboratories) were used as wild type (WT) controls. For acute recordings, animals were aged between 4 and 5 months. All other animals were aged between 3 and 4 months at the time of Neuropixels recordings or perfusion for fixed tissue analyses. Data presented shows the means of both male and female animals.

Immunohistochemistry (IHC)

Brains were extracted from animals after intracardiac perfusion of 1× phosphate-buffered saline (no calcium, no magnesium; PBS; Gibco), post-fixed for 24 h in 4% paraformaldehyde (PFA) in PBS (Alfa Aesar), cryopreserved through increasing sucrose concentrations, embedded in optimal cutting temperature compound (OCT; CellPath), and frozen on dry ice. Amyloid plaque and oligodendrocyte analyses: 10-μm thick sagittal sections were cut using a Leica cryostat. Sections were blocked in blocking solution (10% donkey or goat serum, 0.3% triton in PBS) for 3 h then incubated with Alexa Fluor 594 anti-β-amyloid (Clone 6E10; 1:1,000; BioLegend; 803019), Olig2 (1:500; Millipore; MABN50), ASPA (1:1,000; Sigma-Aldrich; ABN1698), APP (Y188; 1:500; Abcam; ab32136), and/or BACE1 (1:250; Abcam; ab108394) antibodies in block overnight at 4˚C. Where appropriate, sections were washed and incubated with secondary antibodies [Goat anti-Mouse Alexa Fluor 488 (1:1,000; Invitrogen; A11001), Goat anti-Rabbit Alexa Fluor 594 (1:1,000; Invitrogen; A11012), Goat anti-Mouse Alexa Fluor 594 (1:1,000; Invitrogen; A11005), Goat anti-Rabbit Alexa Fluor 488 (1:1,000; Invitrogen; A11008)] in block for 2 h at room temperature (RT). Sections were then labelled with DAPI and mounted with ProLong Gold. Myelin sheath analysis: 30-μm thick coronal brain sections were cut between bregma +1.1 mm and +0.8 mm. Free-floating coronal sections were blocked in 10% fetal calf serum, 0.1% triton in PBS for 1 h then incubated with rat anti-MBP antibody (1:500; Abcam; ab7349) in blocking solution overnight at 4˚C. Sections were washed in PBS before adding Donkey anti-Rat Alexa Fluor 488 secondary antibody (1:1,000; Invitrogen; A21208) for 1 h at RT. Sections were washed and stained for nuclei before being mounted onto slides. Oligodendrocyte autophagy analysis: 40-μm thick free-floating coronal sections were washed in PBS, blocked in M.O.M. blocking solution (Vector laboratories) for 90 min, then incubated in primary antibodies [Olig2 (1:500; Millipore; MABN50), LC3 (1:1,000; Sigma-Aldrich; L7543), Lamp2 (1:2,000; Hybridoma Bank; ABL-93), p62 (1:500; Abcam; ab91526), Ctsd (ThermoFisher; PA5-47046)] overnight at 4˚C. Sections were then washed in PBS followed by incubation with secondary antibodies (Donkey anti-Mouse 488, Donkey anti-Mouse 568, Donkey anti-Rabbit 657, Donkey anti-Rat 488, Donkey anti-Goat 568; all at 1:1,000; Invitrogen) for 2 h at RT. Sections were then washed, labelled with DAPI and mounted onto slides.

Western blotting

Brains were extracted from animals after intracardiac perfusion of 1× PBS, the forebrain was dissected and protein extracted in RIPA buffer (Pierce). Protein in each sample was quantified using a BCA Assay (Pierce) and 20 μg of protein was loaded per well of a NuPAGE 4% to 12% Bis-Tris gel. Samples were run for 1.5 h at 150 V, before transfer to a nitrocellulose membrane using an iBlot 2 transfer system (Thermo Fisher Scientific). Membranes were blocked for 1 h in 1% casein (Bio-Rad) in PBST (0.1% Tween-20 in PBS), then incubated with MBP (1:1,000; Bio-Rad; MCA409S) antibody overnight at 4˚C. Membranes were washed in PBST, incubated with Goat anti-rat ECL antibody (1:10,000; Amersham; NA935) for 1 h, then imaged using Pierce ECL substrate and an Amersham Imager 680. Membranes were subsequently stripped

(Pierce) and reprobed for GAPDH [(1:1,000; Sigma-Aldrich; MAB374); secondary: Sheep anti-mouse ECL (1:10,000; Amersham; NA931)]. Blots were analysed using the Gel Analyzer tools in the FIJI build of ImageJ (open source). Intensity of MBP bands was normalised to the GAPDH band for each lane, and all lanes were normalised to the average of the $App^{NL\text{-}G\text{-}F}$ values.

Neuropixels recordings and analysis

Surgical procedures—Awake recordings. General anaesthesia was induced using approximately 4% isoflurane in O_2 and maintained at approximately 2% throughout the surgery, with anaesthetic depth monitored via the pedal reflex and breathing rate. Carprofen for pain relief was administered by subcutaneous injection prior to surgical procedures. Animals were head fixed in a Mouse Ultra Precise Stereotaxic Instrument (World Precision Instruments, WPI) using ear bars. Normal body temperature was maintained using a heating pad and Viscotears gel applied to the eyes. The scalp was shaved, disinfected with dilute chlorhexidine and cleaned with alcohol, and treated for 5 min with lidocaine cream before skin excision. Following exposure, the skull was first covered with a thin layer of Vetbond (3M), followed by ultraviolet curing Optical Adhesive 81 (Norland), which was cured using a handheld LED UV spot lamp (Intertronics). A craniotomy spanning approximately half the area of the left and right parietal bones between bregma and lambda was drilled using an OmniDrill35 (WPI). A titanium headplate was subsequently attached to the skull behind lambda with SuperBond dental cement (Prestige Dental) and a circular well encircling the exposed skull created using dental cement (Jet, Lang). A layer of sterile PBS was applied to the craniotomy before sealing the well with KwikCast silicone elastomer (WPI). Animals were taken off isoflurane, received a subcutaneous buprenorphine injection for immediate pain relief and were provided with drinking water containing carprofen for 3 days postoperatively. Body weight and score were monitored to ensure appropriate recovery and health of the animal.

Surgical procedures—Acute media injections. Surgical procedures for animals undergoing subsequent acute Neuropixels recordings under isoflurane anaesthesia were conducted as above, but forewent ultraviolet curing and headplate attachment and underwent additional insertion of a silver chloride reference electrode into a small hole drilled over the cerebellum and secured with cyanoacrylate glue and dental cement. These animals were transferred directly to the recording stage at the end of surgical procedures and without interruption of isoflurane anaesthesia.

Recording procedures—Awake. Two weeks post-surgery, mice were put through 3 daily habituation sessions to familiarise them to handling procedures, head fixation apparatus and Neuropixels recording setup. Animals were secured via the implanted headplate in a holder (Thorlabs) suspended above a fixed running wheel fitted with a rotary encoder to monitor locomotion. Behaviour was also monitored via an IR camera filming the head and forelimbs of the animal during Neuropixels recordings. Mice were then lightly sedated with <1% isoflurane, the silicone cap removed, and a silver chloride reference electrode placed in contact with the skull and secured to the edge of the well using dental cement (Jet, Lang). A Neuropixels 1.0 probe (IMEC) was secured to a QUAD micromanipulator (Sutter Instruments) orthogonal to the anterior posterior axis of the mouse at a 60˚ elevation angle and spatially referenced to bregma. The probe was then maneuvered to 2.2 mm posterior and 0.5 mm medial of bregma so as to be inserted into the right hemisphere along a trajectory spanning the retrosplenial cortex and CA1 region of the hippocampus. The probe was then inserted at approximately 10 μm/s along the elevation angle to a depth of 3.2 mm. Following implantation, anaesthesia was removed. Two to three 10-min recordings of spontaneous brain activity sampled at

approximately 30 kHz were taken 40 min after probe implantation. After recordings, the probe was slowly retracted, the reference electrode detached, and well refilled with sterile PBS and KwikCast before animals were returned to their home cage.

Recording procedures—Acute media injections. Following surgical procedures, mice were transferred to the recording stage without interruption of anaesthesia and while remaining in the stereotaxic frame. A 10-μl Hamilton needle syringe, secured to a microinjection pump (UMP3, WPI), was then carefully inserted into retrosplenial cortex (approximately 2 mm AP, 0.5 mm ML) to a depth of approximately 600 μm under micromanipulator control (MM33, Multichannel Systems) and visualised under a microscope (GT Vision). The syringe was preloaded with control media (media conditioned by BACE1 inhibitor-treated oligodendrocytes or media which had been immunodepleted of Aβ; see details below) or oligodendrocyte-conditioned media (media conditioned by vehicle-treated oligodendrocytes grown in parallel, containing 400 to 500 nM of Aβ aggregates, as estimated by aggregate quantification, and 130 pM of $A\beta_{40}$ monomers, as measured by ELISA; see details of media collection and quantification below). Once in position, a Neuropixels probe (IMEC) was secured to a QUAD micromanipulator (Sutter Instruments) and implanted as for awake recordings and as close as possible to the injection needle. Following implantation, the brain was allowed to rest for at least 40 min before subsequent recordings, during which isoflurane anaesthesia was gradually lowered to maintain adequate anaesthetic depth and promote physiological cortical activity (approximately 1%). A single recording of spontaneous brain activity was then performed during which, following a baseline acquisition period of 5 mins, media was injected at a rate of 10 nl/min over 10 min for a total injection volume of 100 nl into retrosplenial cortex. Animals were immediately killed following recordings with no recovery.

Neuropixels analysis. Action potential (i.e., spiking) data (sampling frequency 30 kHz) were separated into individual units using the automated spike sorting algorithm Kilosort3 [56]. For awake recordings, averaged spike waveforms associated with each identified unit were extracted and normalised, and the first and second principal components computed for each waveform (Matlab function "pca"). These metrics were used as inputs to generate a Gaussian mixture distribution model (GMM, Matlab function "fitgmdist," 200 replicates) for subsequent clustering with 2 components (Matlab function "cluster"), with the smallest cluster (typically accounting for $<10\%$ of all unit waveforms and consisting largely of artefactual signals) excluded from further analysis. Remaining waveforms were subsequently visually checked to confirm physiological appearance.

To map identified units to anatomical brain regions, we used custom-written Matlab scripts comprising a modification to the open-source Neuropixels trajectory explorer (https://github.com/petersaj/neuropixels_trajectory_explorer) which incorporates the Allen Common Coordinate Framework (CCF) v3 mouse atlas. This produced a putative anatomical trajectory of the probe with respect to the stereotactic implant coordinates and as a function of the recording channel along the probe shank. To offset this trajectory to account for implantation depth, a depth template of probe channels was created, where cortical and CA1 regions in the predicted trajectory were assigned a nonzero value, with all other areas set to zero. This created a template consisting of 2 square waves that reflects the span of the cortex and CA1 separated by the intervening corpus callosum. The estimated offset was calculated as the largest cross-correlation of this template with a profile of the computed sum of multiunit spiking activity across each recording channel (Matlab function "finddelay"). This calculated offset was then used to align the anatomical trajectory to functional data, so as to assign isolated units to putative brain regions, and visually confirmed.

Behavioural data collected from the IR camera video and rotary encoder were used to separate recordings into different behavioural states. Stationary/quiescent periods were defined as time

points where angular acceleration on the rotary encoder was <0.025 absolute rotations per minute (RPM)/sec and velocity was <0.01 RPM. Non-locomotor movements, such as grooming, whisking, etc., were identified by first calculating the rectified first approximate derivative of the mean intensity value across all pixels in each video frame and defined as signals crossing above 6-fold median absolute deviations. Behavioural data were then split into multiple 1 s windows uninterrupted by locomotion or non-locomotor movements. Windows in which the theta (4 to 8 Hz) – delta (<4 Hz) power ratio remained less than 2 (calculated using the mean LFP across cortical channels, Matlab function "pspectrum," 1-s time resolution with 99% overlap) [57] were subsequently defined as resting state epochs. Spontaneous MFR was calculated for each unit over all identified resting state epochs in each animal across 2 to 3 concatenated Neuropixels recording sessions (mean total duration approximately 28 min). We additionally calculated, for each neuron/unit, the coefficient of variation (CV, standard deviation divided by the mean) of the MFR across resting state epochs ("CV MFR"), as well as the coefficient of variation 2 [58] of the interspike interval (ISI) during quiescent (i.e., non-locomotion) states ("CV2 ISI").

For acute experiments involving local media injections, we calculated the firing rate of all identified units over 1-s bins during the recording period and averaged over the 120-s baseline period prior to media injection, and that during the last 120 s of media injection, to obtain baseline and end-of-injection mean FRs. For each experiment (i.e., animal), the median firing rate across all units was calculated for both baseline and end-of-injection conditions, and the fractional change in median firing rate calculated as ($\text{medianFR}_{end\text{-}of\text{-}injection}$ – $\text{medianFR}_{baseline}$) / $\text{medianFR}_{baseline}$.

Local field potential analysis. Broadband LFP data (sampling frequency 2.5 kHz) were selected from dorsal retrosplenial cortex-associated channels and common average referenced. For each such channel, stationary/quiescent periods were subdivided into complete 60-s epochs and power spectral density estimates for each epoch successively calculated using the multitaper method (Matlab function "pmtm," 7 Discrete Prolate Spheroidal (Slepian) sequences as tapers, <100 Hz), and averaged within and then across recording sessions for each animal. Overall power was subsequently calculated by integrating the associated area using the Simpson's rule (parabolic approximation).

Sharp wave ripple (SWR) analysis. LFP data from CA1 channels were common average referenced and filtered for the ripple band (110 to 250 Hz; fourth-order Butterworth filter with Second-Order-Section implementation for stability) and envelopes/instantaneous amplitudes calculated using the Hilbert transform (Matlab functions "hilbert" and "abs"). SWR events were detected similarly to previously published protocols [59]. Local maxima in the ripple band envelope which exceeded 5 times the median of the envelope values within that channel during quiescence were collated as candidate SWR events. Onset and offset for each event were defined as the nearest time points prior to and following local maxima in which ripple band envelope fell below 50% of the detection threshold, with SWR event time defined as the time of the local maxima. Candidate events were included for final analysis if ripple band power during the event was at least twice as large as that in the common average reference and that of the power in the supra-ripple band (200 to 500 Hz, to account for high frequency noise), occurred when the animal was quiescent and if the theta/delta power ratio was <2 (i.e., during the resting state), and if the event was at least 4 ripple cycles in length and separated from another by at least 500 ms. Similarly to previous protocols [60,61], we next examined the multiunit cortical response to each ripple by computing the ripple triggered peri-event time histograms (PETHs) and counting total spiking activity across all identified dorsal retrosplenial neurons/units in 10-ms bins (range −1 to +1 s). PETHs were smoothed with a 50-ms Gaussian filter, averaged over SWR events across experimental sessions for each animal (minimum of 100 events for inclusion) and z-scored.

Human tissue

The study was carried out in accordance with the Declaration of Helsinki. Postmortem human brain tissue from prefrontal cortex (Brodmann's Area 10) was provided as precut frozen tissue sections by the Queen Square Brain Bank (who obtained the tissue with written informed consent from the donor, next of kin or person with power of attorney) with ethical committee approval (reference UCLMTA4-20), and the tissue is stored under licence from the Human Tissue Authority (licence number 12198). AD tissue is from donors with a clinical diagnosis of sporadic AD and a high level of AD pathological change (A3, B3, C2, or C3). Control tissue is from donors with no clinical diagnosis of neurological disease and no or minimal AD-related pathology. Age: control, 90 ± 7 years (mean ± SD) and AD, 75 ±10; postmortem delay: control, 69 ± 25 h and AD, 59 ± 28; percentage male: control, 50% and AD, 80%.

RNAscope in situ hybridization (ISH)

ISH was carried out using RNAscope Multiplex Fluorescent Kit v2 [Advanced Cell Diagnostics (ACD)] according to the manufacturer's instructions. Briefly, frozen 10-μm thick human tissue sections were dried (4 min at 40˚C then 10 min at RT) before fixation in 4% PFA in PBS (30 min at RT). Sections were then dehydrated through increasing ethanol concentrations (5 min each in 50%, 70%, 100%, 100% ethanol) before incubation with hydrogen peroxide (10 min at RT) followed by incubation with Protease IV (20 min at RT). Hybridization of the probes [Hs-APP (418321; ACD), Hs-BACE1-C2 (422541-C2; ACD), and Hs-MBP-C3 (411051-C3; ACD) or Hs-RBFOX3-C3 (415591-C3; ACD) at a ratio of 50:1:1] was carried out at 40˚C for 2 h. Sections then underwent amplification (30 min at 40˚C for each probe sequentially) followed by sequential detection of each probe [15 min at 40˚C with probe-specific HRP then 30 min at 40˚C with Opal dye (1:500; C1: Opal 570, C2: Opal 620, C3: Opal 520; Akoya Biosciences)]. Following ISH, sections underwent IHC for Aβ: Sections were blocked for 1 h in blocking solution (10% goat serum, 0.1% triton in PBS), incubated with primary antibody in block (anti-β-amyloid clone 6E10; 1:2,000; BioLegend; 803001) overnight at 4˚C, then incubated with secondary antibody in block [Goat anti-Mouse Alexa Fluor 647 (1:1,000; Invitrogen; A21235)] for 2 h at RT. Sections were incubated with TrueBlack (1X; Biotium; 23007) for 30 s and counterstained with DAPI (1:5,000) prior to mounting with ProLong Gold (Invitrogen).

Induced pluripotent stem cells (iPSCs)

iPSCs were previously obtained or generated, and validated, by CA and SW [18,19]. iPSCs were cultured in Essential 8 media on Geltrex and passaged using 0.5 mM EDTA (all reagents from Thermo Fisher). The following cell lines were used in this study: APP V717I 1 (APP V717I mutation), PSEN1 R278I (PSEN1 R278I mutation), PSEN1 int4del (intron 4 deletion in PSEN1), PSEN1 WT (PSEN1 int4del line CRISPR edited to correct the mutation [19]).

iPSC-derived cortical neurons

Cortical neurons were derived from iPSCs as previously described [27]. Briefly, iPSCs underwent neural induction in N2B27 media [1:1 DMEM-F12 Glutamax (Gibco): Neurobasal (Gibco) with 0.5X B27 supplement (Gibco), 0.5X N2 supplement (Gibco), 0.5X Non-essential amino acids (Gibco), 50 μM 2-mercaptoethanol (Gibco), 2.5 μg/ml insulin (Sigma-Aldrich), 50 U/ml Penicillin (Gibco), 50 μg/ml Streptomycin (Gibco), 1 mM L-glutamine (Gibco)] supplemented with 1 μM Dorsomorphin (Tocris) and 10 μM SB-431542 (Generon) for 10 days. Cells were then expanded over 12 to 18 days in neural maintenance media, and split every 6 days using dispase (Gibco) to remove non-neuronal cell types. Cells were then singularised

using accutase (Sigma-Aldrich) before final plating in poly-L-ornithine (Sigma-Aldrich) and laminin (Sigma-Aldrich)-coated wells. Mature cortical neurons begin to appear from 60 days after final plating, and media which had been on the cells for 24 h was collected for Aβ quantification between 120 and 200 days after final plating. To normalise for cell number, cells were lysed at the end of the experiment, total genomic DNA extracted and quantified, and cell number calculated based on each cell containing 6 pg of DNA.

iPSC-derived oligodendrocytes and OPCs

Oligodendrocytes were derived from iPSCs as previously described [17]. Briefly, neural precursor cells (NPCs) were first derived from iPSCs as previously described [27,62]: iPSC colonies were grown in N2B27 media supplemented with 1 μM Dorsomorphin (Tocris), 10 μM SB-431542 (Generon), 3 μM CHIR 99021 (MedChemExpress), and 0.5 μM purmorphamine (Peprotech). After 4 days, Dorsomorphin and SB-431542 were withdrawn and 150 μM ascorbic acid was added. Cells were plated on Geltrex (Gibco) and grown for 30 days, with passaging every 5 to 6 days, to expand and remove contaminating cell types. NPCs were then plated on Geltrex at a density of 100,000 cells/well and expression of *SOX10*, *OLIG2*, and *NKX6.2* was driven by transduction of the cells with SON lentivirus (plasmid kindly provided by Prof. Tanja Kuhlmann, University of Münster; virus constructed by VectorBuilder) at an MOI (multiplicity of infection) of 5, together with 5 μg/ml protamine sulfate (Sigma-Aldrich) for 24 h. Cells were then grown in glial induction medium [GIM; DMEM-F12 glutamax with 0.5X B27 minus vitamin A supplement, 0.5X N2 supplement, 100 U/ml Penicillin, 100 μg/ml Streptomycin, 2 mM L-glutamine, 1 μM SAG (Cayman Chemical), 10 ng/ml PDGF (Peprotech), 10 ng/ml NT3 (Peprotech), 10 ng/ml IGF-1 (Peprotech), 200 μM ascorbic acid, 0.1% Trace Elements B (Corning), 10 ng/ml T3 (Sigma-Aldrich)]. After 4 days, cells were changed into differentiation media [DM; DMEM-F12 glutamax with 0.5X B27 minus vitamin A supplement, 0.5X N2 supplement, 100 U/ml Penicillin, 100 μg/ml Streptomycin, 2 mM L-glutamine, 60 ng/ml T3, 10 ng/ml NT3, 10 ng/ml IGF-1, 200 μM ascorbic acid, 0.1% Trace Elements B, 100 μM dbcAMP (Sigma-Aldrich)]. After 7 to 10 days of differentiation, cells were singularised with accutase and replated on Geltrex at a density of 250,000 cells/well (12-well plate) or 150,000 cells/well (glass coverslips in 24-well plate), and 35 days after glial induction, almost all cells were oligodendroglia ($OLIG2^+$ and/or MBP^+) and cells with mature MBP^+ sheets were visible. Media which had been on the cells for 24 h was collected for Aβ quantification between 40 and 120 days after glial induction. For immature OPCs, cultures were maintained in GIM, and media which had been on the cells for 24 h was collected for Aβ quantification at day 5 after glial induction. To normalise for cell number, cells were lysed at the end of the experiment, total genomic DNA extracted and quantified, and cell number calculated based on each cell containing 6 pg of DNA.

iPSC-derived astrocytes

iPSC-derived astrocytes were generated using an established protocol [63]. Briefly, glial progenitor cells were enriched from cortical neuronal cultures (see above) in a proliferative phase [N2B27 media plus 10 ng/ml FGF2 (Peprotech)] until day 150 of differentiation. During this phase, glial progenitors were routinely passaged using 0.5 mM EDTA and cultured on Geltrex substrate (Thermo Fisher). A final two-week maturation phase consisted of 10 ng/ml LIF (Sigma) and 10 ng/ml BMP4 (Peprotech), at the end of which media which had been on the cells for 24 h was collected for Aβ quantification. To normalise for cell number, cells were lysed at the end of the experiment, total genomic DNA extracted and quantified, and cell number calculated based on each cell containing 6 pg of DNA.

iPSC-derived microglia

iPSC-derived microglial-like cells were generated using established protocols [64,65]. Briefly, embryoid bodies were generated from 10,000 iPSCs and haematopoietic differentiation was initiated via 3 days of 50 ng/ml BMP4, 50 ng/ml VEGF, and 20 ng/ml SCF followed by maintenance in myeloid media consisting of x-vivo media with 25 ng/ml IL3 and 100 ng/ml MCSF. Microglial-like cells were harvested and exposed to a two-week final maturation in 25 ng/ml MCSF, 100 ng/ml IL34, 5 ng/ml TGF-β and further supplemented with CX3CL1 and CD200 for the final 2 days (both 100 ng/ml), at the end of which media was collected for Aβ quantification. All growth factors Peprotech unless stated. To normalise for cell number, cells were lysed at the end of the experiment, total genomic DNA extracted and quantified, and cell number calculated based on each cell containing 6 pg of DNA.

BACE1 inhibitor treatment

BACE1 inhibitor NB-360 (a kind gift from Novartis) was prepared at a concentration of 10 μM in differentiation medium (DM), from a stock solution of 10 mM prepared in dimethyl sulfoxide (DMSO; Sigma-Aldrich). Cells between 40 and 60 days after glial induction which had been in their medium for 24 h had their medium collected (pretreatment) and medium containing 10 μM NB-360 was added. After 24 h of treatment, the medium was collected (posttreatment) and replaced with regular DM. As vehicle controls, cells were in parallel treated with DM containing 0.1% DMSO. Aβ concentrations were quantified in both pretreatment and posttreatment media samples to calculate the change in Aβ production for each well of cells.

DNA extraction

DNA was extracted using the QIAGEN DNeasy Blood and Tissue Kit (69504) according to the manufacturer's instructions. Briefly, cells were collected and suspended in PBS with 10% Proteinase K. Lysis buffer was added and the samples were incubated at 56˚C for 10 min. Ethanol was added and the lysate was added to a DNeasy Mini spin column where the DNA was bound to a membrane. The DNA was twice washed before being eluted. DNA concentrations were measured using a Nanodrop One (Thermo Fisher).

Immunocytochemistry (ICC)

Cells were fixed in 4% PFA in PBS for 10 min, washed in PBS, then incubated with blocking solution (10% goat serum, 2% bovine serum albumin, 0.2% triton in PBS) for 2 h. Cells were then incubated in primary antibodies [MBP (1:50; Abcam; ab7349), OLIG2 (1:100; Atlas Antibodies; HPA003254), GFAP (1:500; Invitrogen; 14-9892-82), anti-Tubulin beta 3 (clone TUJ1; 1:1,000; BioLegend; 801202), IBA1 (1:500; Wako; 019-19741)] in block overnight at 4˚C, washed in PBS, then incubated in secondary antibodies [Goat anti-Rat Alexa Fluor 647 (1:1,000; Invitrogen; A21247), Goat anti-Mouse Alexa Fluor 488 (1:1,000; Invitrogen; A11001), Goat anti-Rabbit Alexa Fluor 594 (1:1,000; Invitrogen; A11012), Goat anti-Rabbit Alexa Fluor 488 (1:1,000; Invitrogen; A11008)] for 1 h at RT. Cells were then labelled with DAPI.

qPCR

Total RNA was extracted from iPSC and iPSC-derived cortical neuron cells using a RNeasy Mini kit (QIAGEN; 74104), including a DNase treatment step, according to the manufacturer's instructions. RNA was reverse-transcribed using a High-Capacity cDNA Reverse Transcription Kit (Applied Biosystems, Carlsbad, California, United States of America) according

to the manufacturer's instructions. Quantitative analysis was carried out using qPCR with gene-specific SYBR green forward (Fwd) and reverse (Rev) primers (*TBR1*: Fwd AGCA GCAAGATCAAAAGTGAGC, Rev ATCCACAGACCCCCTCACTAG; *CTIP2*: Fwd CTCCGAGCTCAGGAAAGTGTC, Rev TCATCTTTACCTGCAATGTTCTCC; *RPL18A*: Fwd CCCACAACATGTACCGGGAA, Rev TCTTGGAGTCGTGGAACTGC) using a Roche LightCycler 480 II. Gene expression in all samples was quantified using the ΔΔCt method normalised first to the housekeeping gene *RPL18A*, then to the average for all iPSC samples.

ELISA

ELISAs for human Aβ40 and human Aβ42 were carried out using commercial kits (Aβ40: Invitrogen KHB3481; Aβ42: Invitrogen KHB3441) according to the manufacturer's instructions. Briefly, samples were added to the wells with capture antibody prebound, together with detection antibody, and incubated for 3 h. Wells were then washed before being incubated with anti-rabbit IgG HRP for 30 min. Wells were again washed, incubated with stabilised chromogen for 30 min, and the reaction stopped. Absorbance at 450 nm was measured using a FLUOstar Omega microplate reader.

Immunodepletion of Aβ

Oligodendrocyte-conditioned media was incubated with anti-Aβ antibody 6E10 (1:500; BioLegend; 803001) for 2 h at 4˚C. Samples were then incubated with prewashed Sepharose Protein A/G beads (50 μl; Rockland; PAG50-00-0002) for 2 h at 4˚C. Beads with bound Aβ and antibody were then removed by centrifugation for 30 s at 12,500 RPM.

Quantification of soluble Aβ aggregates

The technique used to quantify soluble aggregates has previously been validated in multiple studies and has been shown to specifically detect aggregates, and not monomers [29–31]. It relies on the binding of 2 copies of the same antibody (6E10, which only has a single epitope [66]), ensuring that what are detected are at least dimers. The clustering analysis used requires close proximity of at least 2 of these dimers, thus further ensuring that what are detected are aggregates. This method allows quantification of stable assemblies or aggregates at picomolar concentrations, which is a much higher sensitivity than bulk biochemical methods.

Single-molecule pull-down coverslip preparation was performed as previously described [67]. Briefly, neutravidin (0.2 mg/ml) in TBS with 0.05% Tween 20 (TBST) was added to glass coverslips covalently mounted with polyethylene glycol (PEG) and biotin for 10 min, followed by 2 wash steps with TBST and once with TBS with 1% Tween 20 (1%T). Afterwards, biotinylated 6E10 antibody (10 nM; BioLegend; 803007) was added for 15 min, followed by 2 wash steps with TBST and once with 1%T. The media samples were added and incubated overnight at 4˚C followed by 2 wash steps with TBST and once with 1%T. The coverslips were then incubated with 6E10 antibody (500 pM; BioLegend; 803020), labelled with single-strand DNA [68] (ACCACCA) for 45 min, followed by 2 wash steps with TBST and once with 1%T. After washing, TetraSpeck microspheres (1:7,000 in TBS, 10 μl, Thermo Scientific, Cat. T7279) were introduced to each well for 10 min. The TetraSpeck solution was then removed, followed by 2× wash with TBST, and a second PDMS gasket (Merck, GBL-103250-10EA) was stacked on the coverslip before introducing 3 μl of complimentary imaging strand (TGGTGGT- cy3B; atdbio) in TBS. Finally, the coverslip was sealed with another coverslip on top of the second PDMS gasket. Then, the coverslips were imaged on a purpose built [67] TIRF microscope using a 520 nm laser, with 100 milliseconds of exposure for 4,000 frames for each field of view. Three fields of view were acquired from each well. Acquired frames were stacked,

reconstructed, drift corrected, and analysed for the number of aggregates in each field of view, as well as aggregate length using the ACT software [29]. Images of individual aggregates were generated using the ASAP software [69].

Analysis of single nucleus RNA sequencing data

Human single nucleus RNA sequencing data from Zhou and colleagues [10] were obtained via the AD Knowledge Portal (https://adknowledgeportal.org) study snRNAseqAD_TREM2. Human single nucleus RNA sequencing data from Bakken and colleagues [11] were obtained from the Human Protein Atlas (proteinatlas.org). Human single nucleus RNA sequencing data from Mathys and colleagues [5] and Lake and colleagues [12] were obtained from The Myeloid Landscape 2 portal (http://research-pub.gene.com/BrainMyeloidLandscape) [70]. Analysis of Zhou and colleagues dataset: Data analysis was performed using R (4.1.2) and packages Seurat (4.0.6), dplyr (1.0.7), ggplot2 (3.3.5), pheatmap (1.0.12), and wesanderson (0.3.6). For analysis, we retained all cells included in the labelled metadata accompanying the study, without further quality filter. We performed data normalisation, variable gene identification, data scaling, dimensionality reduction with PCA, and clustering analysis using functions implemented in the package Seurat. Subgroups Ex0 and Ex1 were considered together for excitatory neurons and subgroups Oli0 and Oli1 were considered together for oligodendrocytes. The z-score was calculated from the $\log_2$ (normalised counts + 1) and plotted as a heat map for each dataset. Analysis of other 3 datasets: Data for each gene of interest were obtained as normalised counts averaged for each cell type. The z-score was calculated from the $\log_2$ (normalised counts + 1) and plotted as a heat map for each dataset.

Analysis of proteomics data

Protein expression data of isolated mouse brain cells was generated by Sharma and colleagues [14] using Magnetic-Activated Cell Sorting (MACS) to isolate microglia, astrocytes, oligodendrocytes, and neurons from the brains of young (P8) C57/BL6 mice (3 biological replicates), analysed by mass spectrometry. These data were obtained from the journal website. Data for each protein of interest were obtained as $\log_2$ LFQ intensity averaged for each cell type. The z-score was calculated from the $\log_2$ LFQ intensity and plotted as a heat map.

Imaging and analysis

IHC: For oligodendrocyte analysis, sections were imaged using a Zeiss LSM 800 confocal microscope using a 40× magnification (field of view (FOV): 159.73 × 159.73 μm; 2,101 × 2,101 pixels), 4 to 6 FOV from Layers 5/6 of the cortex were captured across 2 to 3 sections, and cells were quantified manually using the FIJI build of ImageJ (open source) after blinding the experimenter to animal genotype. For APP and BACE analysis, sections were imaged using a Zeiss LSM 980 confocal microscope using a 40× magnification, 3 to 4 FOV from the cortex were captured, and cells were quantified manually using the FIJI build of ImageJ (open source). For plaque analysis, sections were imaged using a Zeiss AxioScan slide scanner, capturing the whole of 3 sagittal sections per animal, with a maximum resolution of 0.325 μm/pixel. Images were first manually segmented to select regions of interest [all visible cortical areas (comprising of visual, retrosplenial, and M2 motor areas), Layers 2/3 of motor cortex (M2), Layers 5/6 of motor cortex (M2), Layers 2/3 of retrosplenial cortex, Layers 5/6 of retrosplenial cortex, corpus callosum (including splenium), area CA1 of hippocampus] and remove regions with post-mortem tissue damage or poor imaging quality. The boundary between Layers 2/3 and Layers 5/6 was identified based on the sharp reduction in the density of cell nuclei. Analysis was then automated using the FIJI build of ImageJ software (open source) to segment, count, and

measure $A\beta^+$ plaques. Myelin sheath lengths were analysed as previously described [71,72]: images were captured using a Leica TCS SPE confocal microscope at 20× magnification with a z-step size of 2 μm. Four images were collected from Layer 2/3 of the primary somatosensory cortex from each of 3 sections per animal. Myelin sheaths were measured using the simple neurite trace plug-in for the FIJI build of ImageJ (open source). Only complete myelin sheaths that started and ended within the 30-μm section were traced and measured, and 120 sheaths were measured per mouse. Imaging and analysis was performed blind to genotype/condition. Oligodendrocyte autophagy was analysed as previously described [73,74]: Images were captured using a Zeiss LSM 980 confocal microscope using a 63× magnification (pixel size 0.132 μm) with a z-step size of 0.5 μm, 4 FOV were captured per animal from Layers 5/6 of the cortex, with 2 to 3 cells analysed per FOV. Cells were segmented based on Olig2 staining, the nuclear mask was dilated to capture the cytoplasm, and the fluorescent intensity normalised to surface was measured. Imaging and analysis was performed blind to genotype/condition.

RNAscope: Sections were imaged using a Zeiss LSM 880 or Zeiss LSM 980 confocal microscope using a 40× magnification (FOV: 212.55 × 212.55 μm; 1,024 × 1,024 pixels). Ten FOV were captured from each brain, 5 corresponding to Layer 5/6 of the cortex from different parts of the tissue section and 5 corresponding to Layer 2/3. The number of cells expressing different genes was quantified manually using the FIJI build of ImageJ software (open source) after blinding of the experimenter to the donor ID and diagnosis. Densitometry was carried out using a custom macro in the FIJI build of ImageJ software to segment cell nuclei (rather than algorithmically inferring cell boundaries, which is liable to introduce bias when comparing cell types which greatly differ in size), classify them as MBP^+ or $RBFOX3^+$, and then measure the number and area of BACE1 and APP spots in each cell.

ICC: Cells were imaged using a Zeiss Cell Discoverer 7 imaging system with an LSM 900 confocal imaging module using a 20× magnification (FOV: 202.45 × 202.45 μm; 1,024 × 1,024 pixels). For each line, a minimum of 3 FOV were captured from each of 2 wells. Cell number was quantified manually using a custom macro in the FIJI build of ImageJ software, while cell positivity was assessed manually.

Statistics

Graphs were plotted and statistical tests were carried out using GraphPad Prism software or Matlab. Statistical tests were chosen for each experiment based on the normality of data and sample matching. Actual statistical tests used for each experiment are stated in the figure legends. All statistical tests used were two-sided unless otherwise stated; *n* values stated refer to true biological replicates—depending on the experiment an individual *n* is a human brain (comprising 5 FOV imaged), a cell line (comprising 1 to 4 independent inductions, each of which is the average of 2 to 5 wells), a mouse (comprising 2 to 3 whole sagittal sections imaged or 3 to 12 FOV), or a neuron/unit. Actual *n* values and what they refer to for each experiment are stated in the figure legends.

Supporting information

S1 Fig. Proteins required to produce Aβ are found at high levels in oligodendrocytes. Heatmap showing the $\log_2$ (LFQ intensity) z-score of proteins of interest from isolated mouse astrocytes, microglia, neurons, and oligodendrocytes shows high amounts of APP, BACE1, and PSEN1 in isolated oligodendrocytes. Proteomics data from Sharma and colleagues [14] was generated from cells isolated by Magnetic-Activated Cell Sorting (MACS) from C57/BL6 mice. (TIF)

S2 Fig. Proteins required to produce Aβ are found in the majority of oligodendrocytes. Quantification of immunofluorescent images from 4-month-old wild-type mice (see **Fig 1E and 1F**) showing the percentage of $Olig2^+$ cells which are APP^+ or $BACE1^+$. Each data point represents an individual mouse ($n = 3$) with bars showing mean ± SEM. Source data are available in S1 Data.
(TIF)

S3 Fig. Increase in cells capable of producing Aβ in brains from patients with sporadic AD brains is largely due to oligodendrocytes. (a) Plot showing the number of MBP^+ cells found in Layers 5/6 (**Fig 1A and 1C**) of the prefrontal cortex against the age of the donor. A linear regression analysis indicated no significant relationship ($F(1,7) = 1.958$, $p = 0.2045$), with a low coefficient of determination ($r^2 = 0.2185$), suggesting that age is not a significant contributor to the number of MBP^+ cells in Layers 5/6 of the prefrontal cortex. (**b**) Quantification showing no significant change in the number of oligodendrocytes in Layer 2/3 of the prefrontal cortex of AD brains. (**c**) Quantification showing a significant increase in the number of all Aβ producing cells in sporadic AD (sAD) brains compared to controls. (**d**) Quantification showing a significant increase in the proportion of Aβ producing cells which are oligodendrocytes in sAD brains. (**e**) Quantification of the number of Aβ producing cells which are not oligodendrocytes showing no significant difference between control and AD brains. (**f**) Fluorescent images from Layers 5/6 of control (top) and sporadic AD (sAD; bottom) postmortem human prefrontal cortex labelled for *RBFOX3* (neuron-specific gene; green), *BACE1* (yellow), *APP* (red), Aβ (identified by 6E10-antibody; white), and DAPI (nuclei; blue). Aβ-capable neurons ($RBFOX3^+$ $BACE1^+$ APP^+ nuclei) are marked with white arrowheads. Note the high variability in expression levels of *APP* and *BACE1* between neurons, with high expression in some cells but minimal expression in others. Scale bar = 25 μm. (**g**) Quantification of the proportion of neurons which are capable of producing Aβ. (**h**) Quantification of the number of neurons which are capable of producing Aβ. (**i**) Quantification showing the proportion of Aβ-capable cells which are neurons. Each data point represents a single brain ($n = 4$ control brains, $n = 5$ sAD brains) with bars representing mean ± SEM. Unpaired *t* test; $t(7) = 1.740$, 2.585, 2.467, 1.011, 0.08304, 0.08520, 2.297 in **(b), (c), (d), (e), (g), (h)**, and **(i)**, respectively. Source data are available in S1 Data.
(TIF)

S4 Fig. Densitometric analysis shows increased *APP* and *BACE1* in oligodendrocytes compared to neurons. (**a, b**) Quantification showing more APP^+ (**a**) and $BACE1^+$ (**b**) spots per cell in oligodendrocytes (MBP^+ cells) compared to neurons ($RBFOX3^+$ cells) in both control and sAD human postmortem brains. Each data point represents a single brain ($n = 4$ control brains, $n = 5$ sAD brains) with bars representing mean ± SEM. Two-way repeated measures ANOVA. Cell type effect: (**a**) $F(1,7) = 6.979$; (**b**) $F(1,7) = 5.540$. (**c, d**) Violin plots demonstrating the greater variability in expression levels of *APP* (**c**) and *BACE*1 (**d**) in neurons ($RBFOX3^+$ cells) compared to oligodendrocytes (MBP^+ cells) in human postmortem brains ($n = 843$ MBP^+ cells, $n = 1{,}100$ $RBFOX3^+$ cells from 4 control and 5 sAD brains). Red lines indicate mean, while dotted black lines indicate quartiles. Fligner–Killeen test for equality of variances: $FK(1,1944) = 388.69$, 533.44 in (**c and d**), respectively. Source data are available in S1 Data.
(TIF)

S5 Fig. Human iPSC-derived oligodendrocyte and neuron cultures have high purity. (**a**) Quantification of the proportion of cells in oligodendrocyte cultures which are oligodendrocyte precursor cells (OPCs; $OLIG2^+$ MBP^-) and mature, myelin-expressing oligodendrocytes ($OLIG2^+$ MBP^+) shows that 93.5% ± 2.2% of all cells in these cultures are either

oligodendrocytes or OPCs. Bars show mean + SEM. $n = 3$ cell lines (1 induction per line). (**b**) Separated data from (**a**) showing the quantification of the proportion of cells in oligodendrocyte cultures which OPCs ($OLIG2^+$ MBP^-) and mature, myelin-expressing oligodendrocytes ($OLIG2^+$ MBP^+). Each data point represents an independent differentiation ($n = 1$ per line) with data from each line shown in a different colour, and bars showing mean + SEM. (**c**) Representative fluorescent image of human iPSC-derived oligodendrocyte culture immunolabelled for MBP (green), OLIG2 (red), GFAP (white), and DAPI (blue). No $GFAP^+$ astrocytes were found in 3 out of 3 cultures examined. Scale bar = 25 μm. (**d**) Fluorescent image of human iPSC-derived neuronal culture immunolabelled for the neuronal marker TUJ1 (green) and DAPI (nuclei; blue). Scale bar = 25 μm. (**e**) Quantification of the proportion of cells in neuronal cultures which are neurons shows a high proportion of $TUJ1^+$ cells, consistent with previous studies [75]. Bar shows mean + SEM. $n = 3$ cell lines (1 induction per line). (**f, g**) qPCR data showing high expression of deep cortical layer markers *TBR1* (**f**) and *CTIP2* (**g**) in neuronal cultures compared to undifferentiated iPSCs. Graphs show relative expression of the gene of interest, normalised to the average for iPSC cultures using the ΔΔCt method (with *RPL18A* as the housekeeping gene). Each data point represents a different cell line ($n = 3$; 1 induction per line) with bars showing mean ± SEM. Ratio paired *t* test: $t(2) = 15.73, 4.430$ in (**f and g**), respectively. Source data are available in S1 Data.
(TIF)

S6 Fig. Un-pooled data from iPSC-derived cultures, showing the variability between and within the different cell lines used. (**a**) Un-pooled data from **Fig 3B**: quantification by ELISA showing a significant reduction in the amount of Aβ40 produced (as a % of the amount produced prior to treatment) by human oligodendrocytes when treated with BACE1 inhibitor (NB-360) compared to vehicle control (DMSO). Each data point represents an independent differentiation ($n = 3$ per line) with data from each line shown in a different colour and bars showing mean ± SEM. Two-way repeated measures ANOVA: Treatment effect: $F(1,3) = 468.0$, $p = 0.0002$; Cell line effect: $F(2,3) = 5.987$, $p = 0.0897$. (**b**) Un-pooled data from **Fig 3C**: ELISA data showing more Aβ40 produced by oligodendrocytes than neurons derived from the same human-iPSC lines. Each data point represents an independent differentiation ($n = 3$ per line) with data from each line shown in a different colour and bars showing mean ± SEM. Two-way ANOVA: Cell type effect: $F(1,12) = 6.622$, $p = 0.0244$; Cell line effect: $F(2,12) = 1.984$, $p = 0.1802$. (**c**) Un-pooled data from **Fig 3D**: quantification by ELISA showing higher Aβ42/Aβ40 ratio produced by oligodendrocytes compared to neurons derived from the same fAD human-iPSC lines. Each data point represents an independent differentiation [$n = 4$(PSEN1 WT neurons) or 3 per line] with data from each line shown in a different colour and bars showing mean ± SEM. Two-way ANOVA: Cell type effect: $F(1,13) = 2.058$, $p = 0.1750$; Cell line effect: $F(2,13) = 1.131$, $p = 0.3525$. (**d**) Un-pooled data from **Fig 3F**: quantification showing oligodendrocytes produce a higher proportion of Aβ as aggregates compared to neurons derived from the same human-iPSC lines. Each data point represents an independent differentiation ($n = 3$ per line) with data from each line shown in a different colour and bars showing mean ± SEM. Two-way ANOVA: Cell type effect: $F(1,12) = 13.10$, $p = 0.0035$; Cell line effect: $F(2,12) = 1.289$, $p = 0.3112$. Source data are available in S1 Data.
(TIF)

S7 Fig. Immature OPCs, astrocytes and microglia produce low amounts of Aβ. (**a–f**) Representative fluorescent images (**a, c, e**) and quantifications showing characterisation of OPC (**a, b**), astrocyte (**c, d**), and microglia (**e, f**) cultures. In (**a**), cells are immunolabelled for MBP (myelin basic protein; green), OLIG2 (marker of all oligodendroglia; red), and DAPI (nuclei; blue), with quantification in (**b**) showing 96.8% ± 0.2% of cells are $OLIG2^+$ MBP^- OPCs while

there are no mature MBP^+ oligodendrocytes. In (**c**), cells are immunolabelled for GFAP (green) and DAPI (blue), with quantification in (**d**) showing 88.3% ±1.0% of cells are $GFAP^+$ astrocytes. In (**e**), cells are immunolabelled for IBA1 (green) and DAPI (blue), with quantification in (**f**) showing 95.9% ± 0.2% of cells are $IBA1^+$ microglia. In (**a, c, e**), scale bar = 25 μm. In (**b, d, f**) bars show mean + SEM, $n = 2$ cell lines (1 induction per line). (**g**) ELISA data showing very low amounts of $A\beta_{40}$ produced by human iPSC-derived OPCs, astrocytes, and microglia compared to neurons and oligodendrocytes. Each data point represents the average of 2 (OPCs, astrocytes, microglia) or 3 (neurons, oligodendrocytes) independent inductions/harvests from a different cell line (OPCs, astrocytes, microglia: $n = 2$; neurons, oligodendrocytes: $n = 3$), with bars representing mean ± SEM. Mixed effects analysis ($F(4,5) = 27.77$, $p = 0.013$) with Dunnet's post hoc tests. Source data are available in S1 Data.
(TIF)

S8 Fig. A majority of soluble Aβ aggregates produced by human neurons and oligodendrocytes are between 20 nm and 200 nm. (**a, b**) Examples of super-resolved aggregates detected in neuronal media (**a**) and oligodendrocyte media (**b**). Scale bar = 50 nm. (**c**) Cumulative frequency histogram showing the size distribution of aggregates produced by neurons and oligodendrocytes (bin size = 10 nm). Source data are available in S1 Data.
(TIF)

S9 Fig. Genetic suppression of BACE1 in oligodendrocytes after 4 weeks of age does not affect total amount of MBP or myelin sheath length. (**a**) Western blot for MBP (top) and GAPDH loading control (bottom) on forebrain homogenates from $App^{NL\text{-}G\text{-}F}$ mice (left 3 lanes), and $App^{NL\text{-}G\text{-}F}$ mice with BACE1 knocked out (KO) specifically in oligodendrocytes (Oligo-KO; middle 3 lanes) or neurons (Neuron-KO; right 3 lanes). (**b**) Quantification of the MBP bands normalised to GAPDH loading control shows no significant difference in MBP levels in mice with BACE1 knocked out. In (**b**), data points represent individual mice ($n = 3$ per group) with bars showing mean ± SEM. One-way ANOVA: $F(2,6) = 0.1924$, $p = 0.8299$. (**c**) Representative immunofluorescent images of myelin sheaths (labelled with MBP, green) in the sparsely myelinated Layers 2/3 of the primary somatosensory cortex showing no significant differences between $App^{NL\text{-}G\text{-}F}$ mice (left) and $App^{NL\text{-}G\text{-}F}$ mice with BACE1 KO specifically in oligodendrocytes (Oligo-KO; right). Coloured pairs of arrows indicate the start and end of example myelin sheaths. Scale bar = 30 μm. (**d**) Quantification of the lengths of myelin sheaths in the cortex, as previously described [71,72], shows no differences in mice with BACE1 knocked out after 4 weeks of age. In (**d**), each data point represents the average of 120 myelin sheaths measured from an individual mouse ($n = 4$ per group) with bars showing mean ± SEM. Unpaired t test: $t(6) = 0.4259$. Source data are available in S1 Data.
(TIF)

S10 Fig. Genetic suppression of BACE1 in oligodendrocytes after 4 weeks of age has no significant effect on oligodendrocyte number. (**a**) Immunofluorescent images showing pan-oligodendroglial marker Olig2 (green), oligodendrocyte-specific marker ASPA (red), and DAPI (blue) in the cortex of $App^{NL\text{-}G\text{-}F}$ control mice (top) and $App^{NL\text{-}G\text{-}F}$ mice with BACE1 KO specifically in oligodendrocytes (bottom). Scale bar = 25 μm. (**b**) Quantification of $Olig2^+$ $ASPA^+$ cells shows no significant difference in oligodendrocyte number in mice with BACE1 KO. (**c**) Quantification of $Olig2^+$ $ASPA^-$ cells shows no significant difference in the number of oligodendrocyte precursor cells (OPCs) in mice with BACE1 KO. In (**b and c**), data points represent individual mice ($n = 4$ per group) with bars showing mean ± SEM. One-way ANOVA: $F(3,12) = 0.04745$, 0.6279; $p = 0.9856$, 0.6107 in (**b and c**), respectively. Source data are available in S1 Data.
(TIF)

S11 Fig. Genetic suppression of BACE1 in oligodendrocytes of *App*$^{NL\text{-}G\text{-}F}$ mice after 4 weeks of age has no significant effect on oligodendrocyte autophagy [73,74]. (**a**) Immunofluorescent images showing oligodendroglial marker Olig2 (yellow), autophagosome marker MAP1LC3B/LC3B (microtubule-associated protein 1 light chain β; LC3; cyan), lysosome protease Cathepsin-d (Ctsd; magenta), and nuclear marker DAPI (white) in the cortex of WT (top), *App*$^{NL\text{-}G\text{-}F}$ control mice (middle), and *App*$^{NL\text{-}G\text{-}F}$ mice with BACE1 KO specifically in oligodendrocytes (Oligo-KO; bottom). (**b, c**) Quantification shows no significant changes in LC3 (**b**), or Ctsd (**c**) within oligodendroglia upon knockout of BACE1 in oligodendrocytes. (**d**) Immunofluorescent images showing oligodendroglial marker Olig2 (yellow), autophagy adapter Sqstm1/p62 (cyan), lysosome marker Lamp2 (lysosome-associated membrane protein 2; magenta), and nuclear marker DAPI (white) in the cortex of WT (top), *App*$^{NL\text{-}G\text{-}F}$ control mice (middle), and *App*$^{NL\text{-}G\text{-}F}$ mice with BACE1 KO specifically in oligodendrocytes (Oligo-KO; bottom). (**e, f**) Quantification shows no significant changes in p62 (**e**), or Lamp2 (**f**) within oligodendroglia upon knockout of BACE1 in oligodendrocytes. In (**b–c and e–f**), data points represent individual mice ($n = 3$ WT in **e and f**, $n = 4$ for all other groups) with bars showing mean ± SEM. One-way ANOVA: $F(2,9) = 1.207, 0.5826$; $p = 0.3434, 0.5782$ in (**b and c**), respectively. $F(2,8) = 0.7969, 0.01823$; $p = 0.4835, 0.9820$ in (**e and f**), respectively. Source data are available in S1 Data.
(TIF)

S12 Fig. Genetic suppression of oligodendrocyte Aβ production leads to a modest reduction in Aβ plaque burden while genetic suppression of neuronal Aβ production eliminates plaques in all regions examined of the *App*$^{NL\text{-}G\text{-}F}$ mouse model of AD. (**a, e**) Quantification of plaque number (**a**) and plaque area (**e**) across different layers of the retrosplenial cortex suggests that oligodendrocyte specific KO of BACE1 leads to a greater reduction in plaque pathology in deeper layers (Layers 5/6) than is observed in superficial layers (Layers 2/3). Data points represent individual mice ($n = 7$ *App*$^{NL\text{-}G\text{-}F}$, 7 Oligo-KO, 4 Neuron-KO) with bars showing mean ± SEM. Two-way repeated measures ANOVA with Tukey's post hoc tests. BACE1 KO effect: $F(2,15) = 61.25$ (**a**), 22.59 (**e**); $p < 0.0001$ (all); Layer-BACE1 KO interaction effect: $F(2,15) = 0.8174$ (**a**), 5.892 (**e**); $p = 0.4603$ (**a**), $p = 0.0129$ (**e**). (**b, f**) Quantification of plaque number (**b**) and plaque area (**f**) across different layers of the motor cortex. Data points represent individual mice ($n = 8$ *App*$^{NL\text{-}G\text{-}F}$, 6 Oligo-KO, 4 Neuron-KO) with bars showing mean ± SEM. Two-way repeated measures ANOVA with Tukey's post hoc tests. BACE1 KO effect: $F(2,15) = 47.58$ (**b**), 13.24 (**f**); $p < 0.0001$ (**b**), $p = 0.0005$ (**f**); Layer-BACE1 KO interaction effect: $F(2,15) = 0.2164$ (**b**), 0.9289 (**f**); $p = 0.8079$ (**b**), $p = 0.4166$ (**f**). (**c, d, g, h**) Quantification of plaque number (**c, d**) and plaque area (**g, h**) in the corpus callosum (**c, g**) and hippocampal area CA1 (**d, h**) shows a trend towards reduction in Oligo-KO mice in these regions. In (**c, g**), data points represent individual mice ($n = 8$ *App*$^{NL\text{-}G\text{-}F}$, 7 Oligo-KO, 4 Neuron-KO) with bars showing mean ± SEM. One-way ANOVA with Dunnet's post hoc tests: $F(2,16) = 12.94, 7.549$; $p = 0.0005, 0.0049$ in (**c, g**), respectively. In (**d, h**), data points represent individual mice ($n = 8$ *App*$^{NL\text{-}G\text{-}F}$, 9 Oligo-KO, 4 Neuron-KO) with bars showing mean ± SEM. One-way ANOVA with Dunnet's post hoc tests: $F(2,18) = 21.83, 9.338$; $p < 0.0001$, $p = 0.0017$ in (**g, h**) respectively. Source data are available in S1 Data.
(TIF)

S13 Fig. Oligodendrocyte-specific knockout of BACE1 in *App*$^{NL\text{-}G\text{-}F}$ mice restores the temporal structure of neuronal firing to levels seen in WT controls. (**a**) Cumulative frequency distribution of the coefficient of variation (CV) of the mean firing rate (MFR) shows that variability in MFR during rest is restored to WT levels in *App*$^{NL\text{-}G\text{-}F}$ mice with BACE1 knocked out (KO) specifically in oligodendrocytes (Oligo-KO; WT vs. Oligo-KO: $p = 0.6192$). (**b**)

Cumulative frequency distribution of the coefficient of variation 2 (CV2) of the inter-spike interval (ISI) shows the restoration of spike train variability to WT levels in Oligo-KO mice (WT vs. Oligo-KO: $p = 0.5032$) during quiescence. In (**a**), individual neurons/units are plotted ($n = 82$ WT, 134 $App^{NL\text{-}G\text{-}F}$, 165 Oligo-KO, 75 Neuron-KO) from 4 (WT) or 3 mice per group. Kolmogrov–Smirnov tests ($D = 0.2026$ (WT vs. $App^{NL\text{-}G\text{-}F}$), 0.2688 ($App^{NL\text{-}G\text{-}F}$ vs. Oligo-KO), 0.2088 ($App^{NL\text{-}G\text{-}F}$ vs. Neuron-KO)). In (**b**) individual neurons/units are plotted ($n = 81$ WT, 134 $App^{NL\text{-}G\text{-}F}$, 165 Oligo-KO, 68 Neuron-KO) from 4 (WT) or 3 mice per group. Kolmogrov–Smirnov tests ($D = 0.1891$ (WT vs. $App^{NL\text{-}G\text{-}F}$), 0.1787 ($App^{NL\text{-}G\text{-}F}$ vs. Oligo-KO), 0.2215 ($App^{NL\text{-}G\text{-}F}$ vs. Neuron-KO)). Source data are available in S1 Data.
(TIF)

S14 Fig. No significant effect on local field potentials following BACE1 knockout in $App^{NL\text{-}G\text{-}F}$ mice. Power spectrum of local field potential (LFP) recordings in retrosplenial cortex showing no major differences between genotypes. $n = 4$ (WT), 3 (other groups) mice. One-way ANOVA: $F(3,9) = 0.6235$, $p = 0.6175$. Source data are available in S1 Data.
(TIF)

S15 Fig. No significant effect on cortical responses to sharp-wave ripple events in CA1 following BACE1 knockout in $App^{NL\text{-}G\text{-}F}$ mice. (**a**) Schematic illustrating a typical cortical multiunit response (top; black) to a sharp wave ripple (SWR) event in CA1 (bottom; blue). (**b**) Trace of the averaged cortical multiunit responses to CA1 SWR events showing no significant differences between genotypes in amplitude [peak z-score; one-way ANOVA: $F(3,8) = 1.008$, $p = 0.4381$] or timing [delay time of centre of mass; one-way ANOVA: $F(3,8) = 1.186$, $p = 0.3745$]. $n = 4$ (WT), 3 ($App^{NL\text{-}G\text{-}F}$, Oligo-KO), 2 (Neuron-KO) mice. Source data are available in S1 Data.
(TIF)

S16 Fig. Seizure 6 protein (*SEZ6*) is expressed at high levels in neurons, but not in oligodendrocytes. Heatmap showing the $\log_2$ (norm count) z-score of *SEZ6* across different cell types from 3 different datasets [5,10–12]. [OPCs: oligodendrocyte precursor cells].
(TIF)

S1 Data. Source data for graphs within this manuscript. Excel spreadsheet containing, in separate sheets, the underlying numerical data for figure panels 2B–2D, 3B–3D, 3F–3F, 4B–4C, 5B, 5D, S2, S3A–S3E, S3G–S3I, S4A–S4D, S5A–S5B, S5E–S5G, S6A–S6D, S7B, S7D, S7F–S7G, S8C, S9B, S9D, S10B–S10C, S11B–S11C, S11E–S11F, S12A–S12H, S13A–S13B, S14, S15.
(XLSX)

S1 Raw Images. Raw images of western blot in S9A Fig.
(PDF)

Acknowledgments

We thank David Attwell, Siddharthan Chandran, Bart De Strooper, and James Rowland for comments on the manuscript. We thank UK DRI at UCL technical staff Elena Ghirardello and Phillip Muckett for the maintenance of animal colonies and assistance with animal experiments. We thank the Queen Square Brain Bank for Neurological Disorders for provision of human brain tissue samples. The Queen Square Brain Bank is supported by the Reta Lila Weston Institute of Neurological Studies, UCL Queen Square Institute of Neurology. We thank Tanja Kuhlmann and the University of Münster for providing the SON lentivirus. We thank Takashi Saito and Takaomi C. Saido for provision of $App^{NL\text{-}G\text{-}F}$ mice. We thank Ulf Neumann and Derya Shimshek from Novartis for providing us with the BACE1 inhibitor NB-360.

Author Contributions

Conceptualization: Rikesh M. Rajani, Carlo Sala Frigerio, Marc Aurel Busche.

Data curation: Rikesh M. Rajani, Marc Aurel Busche.

Formal analysis: Rikesh M. Rajani, Robert Ellingford, Mariam Hellmuth, Samuel S. Harris, Emre Fertan, John S. H. Danial, Matthew Swire, Marcus Lloyd, Mathieu Bourdenx, Carlo Sala Frigerio.

Funding acquisition: Rikesh M. Rajani, Carlo Sala Frigerio, Marc Aurel Busche.

Investigation: Rikesh M. Rajani, Robert Ellingford, Mariam Hellmuth, Samuel S. Harris, Orjona S. Taso, David Graykowski, Francesca Kar Wey Lam, Charles Arber, Emre Fertan, John S. H. Danial, Matthew Swire, Marcus Lloyd, Tatiana A. Giovannucci, Mathieu Bourdenx.

Methodology: Rikesh M. Rajani, Robert Ellingford, Samuel S. Harris, Orjona S. Taso, Charles Arber, Emre Fertan, John S. H. Danial, Matthew Swire, Tatiana A. Giovannucci, Mathieu Bourdenx.

Project administration: Rikesh M. Rajani, Marc Aurel Busche.

Resources: Charles Arber, Robert Vassar, Selina Wray.

Software: Samuel S. Harris.

Supervision: Rikesh M. Rajani, David Klenerman, Selina Wray, Carlo Sala Frigerio, Marc Aurel Busche.

Validation: Rikesh M. Rajani.

Visualization: Rikesh M. Rajani, Samuel S. Harris.

Writing – original draft: Rikesh M. Rajani, Marc Aurel Busche.

Writing – review & editing: Rikesh M. Rajani, Robert Ellingford, Mariam Hellmuth, Samuel S. Harris, Orjona S. Taso, David Graykowski, Francesca Kar Wey Lam, Charles Arber, Emre Fertan, John S. H. Danial, Marcus Lloyd, Tatiana A. Giovannucci, Mathieu Bourdenx, David Klenerman, Robert Vassar, Selina Wray, Carlo Sala Frigerio, Marc Aurel Busche.

References

1. van Dyck CH, Swanson CJ, Aisen P, Bateman RJ, Chen C, Gee M, et al. Lecanemab in Early Alzheimer's Disease. N Engl J Med. 2022;1–13. https://doi.org/10.1056/NEJMoa2212948 PMID: 36449413
2. Sims JR, Zimmer JA, Evans CD, Lu M, Ardayfio P, Sparks J, et al. Donanemab in Early Symptomatic Alzheimer Disease. JAMA. 2023; 46285:1–16. https://doi.org/10.1001/jama.2023.13239 PMID: 37459141
3. Busche MA, Eichhoff G, Adelsberger H, Abramowski D, Wiederhold K-H, Haass C, et al. Clusters of Hyperactive Neurons Near Amyloid Plaques in a Mouse Model of Alzheimer's Disease. Science (80-). 2008; 321:1686–1689. https://doi.org/10.1126/science.1162844 PMID: 18802001
4. Giorgio J, Adams JN, Maass A, Jagust WJ, Giorgio J, Adams JN, et al. Article Amyloid induced hyperexcitability in default mode network drives medial temporal hyperactivity and early tau accumulation Amyloid induced hyperexcitability in default mode network drives medial temporal hyperactivity and early tau accumulation. Neuron. 2024;1–11. https://doi.org/10.1016/j.neuron.2023.11.014 PMID: 38096815
5. Mathys H, Davila-Velderrain J, Peng Z, Gao F, Mohammadi S, Young JZ, et al. Single-cell transcriptomic analysis of Alzheimer's disease. Nature. 2019; 570:332–337. https://doi.org/10.1038/s41586-019-1195-2 PMID: 31042697
6. Sadick JSO'Dea MR, Hasel P, Dykstra T, Faustin A, Liddelow SA. Astrocytes and oligodendrocytes undergo subtype-specific transcriptional changes in Alzheimer's disease. Neuron. 2022; 110:1788–1805.e10. https://doi.org/10.1016/j.neuron.2022.03.008 PMID: 35381189

7. Chen WT, Lu A, Craessaerts K, Pavie B, Sala Frigerio C, Corthout N, et al. Spatial Transcriptomics and In Situ Sequencing to Study Alzheimer's Disease. Cell. 2020; 182:976–991.e19. https://doi.org/10.1016/j.cell.2020.06.038 PMID: 32702314

8. Park H, Cho B, Kim H, Saito T, Saido TC, Won KJ, et al. Single-cell RNA-sequencing identifies disease-associated oligodendrocytes in male APP NL-G-F and 5XFAD mice. Nat Commun. 2023; 14:1–14. https://doi.org/10.1038/s41467-022-34464-6

9. Graham AC, Bellou E, Harwood JC, Yaman U, Celikag M, Magusali N, et al. Genetic variation associated with human longevity and Alzheimer's disease risk act through microglia and oligodendrocyte cross-talk. medRxiv. 2023. https://doi.org/10.1101/2023.03.30.23287975

10. Zhou Y, Song WM, Andhey PS, Swain A, Levy T, Miller KR, et al. Human and mouse single-nucleus transcriptomics reveal TREM2-dependent and TREM2-independent cellular responses in Alzheimer's disease. Nat Med. 2020; 26:131–142. https://doi.org/10.1038/s41591-019-0695-9 PMID: 31932797

11. Bakken TE, Jorstad NL, Hu Q, Lake BB, Tian W, Kalmbach BE, et al. Comparative cellular analysis of motor cortex in human, marmoset and mouse. Nature. 2021; 598:111–119. https://doi.org/10.1038/s41586-021-03465-8 PMID: 34616062

12. Lake BB, Chen S, Sos BC, Fan J, Kaeser GE, Yung YC, et al. Integrative single-cell analysis of transcriptional and epigenetic states in the human adult brain. Nat Biotechnol. 2018; 36:70–80. https://doi.org/10.1038/nbt.4038 PMID: 29227469

13. Herreman A, Hartmann D, Annaert W, Saftig P, Craessaerts K, Serneels L, et al. Presenilin 2 deficiency causes a mild pulmonary phenotype and no changes in amyloid precursor protein processing but enhances the embryonic lethal phenotype of presenilin 1 deficiency. Proc Natl Acad Sci U S A. 1999; 96:11872–11877. https://doi.org/10.1073/pnas.96.21.11872 PMID: 10518543

14. Sharma K, Schmitt S, Bergner CG, Tyanova S, Kannaiyan N, Manrique-Hoyos N, et al. Cell type- and brain region-resolved mouse brain proteome. Nat Neurosci. 2015; 18:1819–1831. https://doi.org/10.1038/nn.4160 PMID: 26523646

15. Zhang Y, Sloan SA, Clarke LE, Caneda C, Plaza CA, Blumenthal PD, et al. Purification and Characterization of Progenitor and Mature Human Astrocytes Reveals Transcriptional and Functional Differences with Mouse. Neuron. 2016; 89:37–53. https://doi.org/10.1016/j.neuron.2015.11.013 PMID: 26687838

16. Depp C, Sun T, Sasmita AO, Spieth L, Berghoff SA, Nazarenko T, et al. Myelin dysfunction drives amyloid-β deposition in models of Alzheimer's disease. Nature. 2023; 618:349–357. https://doi.org/10.1038/s41586-023-06120-6 PMID: 37258678

17. Ehrlich M, Mozafari S, Glatza M, Starost L, Velychko S, Hallmann A-L, et al. Rapid and efficient generation of oligodendrocytes from human induced pluripotent stem cells using transcription factors. Proc Natl Acad Sci. 2017; 114:E2243–E2252. https://doi.org/10.1073/pnas.1614412114 PMID: 28246330

18. Arber C, Toombs J, Lovejoy C, Ryan NS, Paterson RW, Willumsen N, et al. Familial Alzheimer's disease patient-derived neurons reveal distinct mutation-specific effects on amyloid beta. Mol Psychiatry. 2020; 25:2919–2931. https://doi.org/10.1038/s41380-019-0410-8 PMID: 30980041

19. Arber C, Villegas-Llerena C, Toombs J, Pocock JM, Ryan NS, Fox NC, et al. Amyloid precursor protein processing in human neurons with an allelic series of the PSEN1 intron 4 deletion mutation and total presenilin-1 knockout. Brain Commun. 2019; 1:1–10. https://doi.org/10.1093/braincomms/fcz024 PMID: 32395715

20. Neumann U, Rueeger H, MacHauer R, Veenstra SJ, Lueoend RM, Tintelnot-Blomley M, et al. A novel BACE inhibitor NB-360 shows a superior pharmacological profile and robust reduction of amyloid-β and neuroinflammation in APP transgenic mice. Mol Neurodegener. 2015; 10:1–15. https://doi.org/10.1186/s13024-015-0033-8 PMID: 26336937

21. Hung COY, Livesey FJ. Altered γ-Secretase Processing of APP Disrupts Lysosome and Autophagosome Function in Monogenic Alzheimer's Disease. Cell Rep. 2018; 25:3647–3660.e2. https://doi.org/10.1016/j.celrep.2018.11.095 PMID: 30590039

22. Cusulin C, Wells I, Badillo S, Duran-Pacheco GC, Baumann K, Patsch C. Gamma secretase modulators and BACE inhibitors reduce Aβ production without altering gene expression in Alzheimer's disease iPSC-derived neurons and mice. Mol Cell Neurosci. 2019; 100:103392. https://doi.org/10.1016/j.mcn.2019.103392 PMID: 31381983

23. Arber C, Lovejoy C, Harris L, Willumsen N, Alatza A, Casey JM, et al. Familial Alzheimer's Disease Mutations in PSEN1 Lead to Premature Human Stem Cell Neurogenesis. Cell Rep. 2021; 34:108615. https://doi.org/10.1016/j.celrep.2020.108615 PMID: 33440141

24. Moore S, Evans LDB, Andersson T, Portelius E, Smith J, Dias TB, et al. APP Metabolism Regulates Tau Proteostasis in Human Cerebral Cortex Neurons. Cell Rep. 2015; 11:689–696. https://doi.org/10.1016/j.celrep.2015.03.068 PMID: 25921538

25. Skaper SD, Evans NA, Soden PE, Rosin C, Facci L, Richardson JC. Oligodendrocytes are a novel source of amyloid peptide generation. Neurochem Res. 2009; 34:2243–2250. https://doi.org/10.1007/s11064-009-0022-9 PMID: 19557514

26. Gazestani V, Kamath T, Nadaf NM, Dougalis A, Burris SJ, Rooney B, et al. Early Alzheimer's disease pathology in human cortex involves transient cell states. Cell. 2023; 186:4438–4453.e23. https://doi.org/10.1016/j.cell.2023.08.005 PMID: 37774681

27. Shi Y, Kirwan P, Livesey FJ. Directed differentiation of human pluripotent stem cells to cerebral cortex neurons and neural networks. Nat Protoc. 2012; 7:1836–1846. https://doi.org/10.1038/nprot.2012.116 PMID: 22976355

28. Haass C, Selkoe DJ. Soluble protein oligomers in neurodegeneration: Lessons from the Alzheimer's amyloid β-peptide. Nat Rev Mol Cell Biol. 2007; 8:101–112. https://doi.org/10.1038/nrm2101 PMID: 17245412

29. Xia Z, Wu Y, Lam JYL, Zhang Z, Burke M, Fertan E, et al. A computational suite for the structural and functional characterization of amyloid aggregates. Cell Reports Methods. 2023; 3:100499. https://doi.org/10.1016/j.crmeth.2023.100499 PMID: 37426747

30. Fertan E, Böken D, Murray A, Danial JSH, Lam JYL, Wu Y, et al. Cerebral organoids with chromosome 21 trisomy secrete Alzheimer's disease-related soluble aggregates detectable by single-molecule-fluorescence and super-resolution microscopy. Mol Psychiatry. 2023;1–18. https://doi.org/10.1038/s41380-023-02333-3 PMID: 38102482

31. Danial JSH, Lam JYL, Wu Y, Woolley M, Dimou E, Cheetham MR, et al. Constructing a cost-efficient, high-throughput and high-quality single-molecule localization microscope for super-resolution imaging. Nat Protoc. 2022; 17:2570–2619. https://doi.org/10.1038/s41596-022-00730-6 PMID: 36002768

32. Stern AM, Yang Y, Jin S, Yamashita K, Meunier AL, Liu W, et al. Abundant Aβ fibrils in ultracentrifugal supernatants of aqueous extracts from Alzheimer's disease brains. Neuron. 2023; 111:2012–2020.e4. https://doi.org/10.1016/j.neuron.2023.04.007 PMID: 37167969

33. Saito T, Matsuba Y, Mihira N, Takano J, Nilsson P, Itohara S, et al. Single App knock-in mouse models of Alzheimer's disease. Nat Neurosci. 2014; 17:661–663. https://doi.org/10.1038/nn.3697 PMID: 24728269

34. Hu X, Hicks CW, He W, Wong P, Macklin WB, Trapp BD, et al. Bace1 modulates myelination in the central and peripheral nervous system. Nat Neurosci. 2006; 9:1520–1525. https://doi.org/10.1038/nn1797 PMID: 17099708

35. Hamano K, Takeya T, Iwasaki N, Nakayama J, Ohto T, Okada Y. A quantitative study of the progress of myelination in the rat central nervous system, using the immunohistochemical method for proteolipid protein. Dev Brain Res. 1998; 108:287–293. https://doi.org/10.1016/s0165-3806(98)00063-7 PMID: 9693804

36. Ou-Yang M-H, Kurz JE, Nomura T, Popovic J, Rajapaksha TW, Dong H, et al. Axonal organization defects in the hippocampus of adult conditional BACE1 knockout mice. Sci Transl Med. 2018;10. https://doi.org/10.1126/scitranslmed.aao5620 PMID: 30232227

37. Buckner RL, Snyder AZ, Shannon BJ, LaRossa G, Sachs R, Fotenos AF, et al. Molecular, structural, and functional characterization of Alzheimer's disease: Evidence for a relationship between default activity, amyloid, and memory. J Neurosci. 2005; 25:7709–7717. https://doi.org/10.1523/JNEUROSCI.2177-05.2005 PMID: 16120771

38. Keskin AD, Kekuš M, Adelsberger H, Neumann U, Shimshek DR, Song B, et al. BACE inhibition-dependent repair of Alzheimer's pathophysiology. Proc Natl Acad Sci U S A. 2017; 114:8631–8636. https://doi.org/10.1073/pnas.1708106114 PMID: 28739891

39. Busche MA, Chen X, Henning HA, Reichwald J, Staufenbiel M, Sakmann B, et al. Critical role of soluble amyloid-β for early hippocampal hyperactivity in a mouse model of Alzheimer's disease. Proc Natl Acad Sci U S A. 2012; 109:8740–8745. https://doi.org/10.1073/pnas.1206171109 PMID: 22592800

40. Zott B, Simon MM, Hong W, Unger F, Chen-Engerer HJ, Frosch MP, et al. A vicious cycle of β amyloid −dependent neuronal hyperactivation. Science (80-). 2019; 365:559–565. https://doi.org/10.1126/science.aay0198 PMID: 31395777

41. Khodagholy D, Gelinas JN, Buzsáki G. Learning-enhanced coupling between ripple oscillations in association cortices and hippocampus. Science (80-). 2017; 358:369–372. https://doi.org/10.1126/science.aan6203 PMID: 29051381

42. Snyder SW, Ladror US, Wade WS, Wang GT, Barrett LW, Matayoshi ED, et al. Amyloid-beta aggregation: selective inhibition of aggregation in mixtures of amyloid with different chain lengths. Biophys J. 1994; 67:1216–1228. https://doi.org/10.1016/S0006-3495(94)80591-0 PMID: 7811936

43. Kuperstein I, Broersen K, Benilova I, Rozenski J, Jonckheere W, Debulpaep M, et al. Neurotoxicity of Alzheimer's disease Aβ peptides is induced by small changes in the Aβ42 to Aβ40 ratio. EMBO J. 2010; 29:3408–3420. https://doi.org/10.1038/emboj.2010.211 PMID: 20818335

44. Iljina M, Garcia GA, Dear AJ, Flint J, Narayan P, Michaels TCT, et al. Quantitative analysis of co-oligomer formation by amyloid-beta peptide isoforms. Sci Rep. 2016; 6:1–8. https://doi.org/10.1038/srep28658 PMID: 27346247

45. Lee JH, Yang DS, Goulbourne CN, Im E, Stavrides P, Pensalfini A, et al. Faulty autolysosome acidification in Alzheimer's disease mouse models induces autophagic build-up of Aβ in neurons, yielding senile plaques. Nat Neurosci. 2022; 25:688–701. https://doi.org/10.1038/s41593-022-01084-8 PMID: 35654956

46. Pensalfini A, Albay R, Rasool S, Wu JW, Hatami A, Arai H, et al. Intracellular amyloid and the neuronal origin of Alzheimer neuritic plaques. Neurobiol Dis. 2014; 71:53–61. https://doi.org/10.1016/j.nbd.2014.07.011 PMID: 25092575

47. D'Andrea MR, Nagele RG, Wang HY, Peterson PA, Lee DHS. Evidence that neurones accumulating amyloid can undergo lysis to form amyloid plaques in Alzheimer's disease. Histopathology. 2001; 38:120–134. https://doi.org/10.1046/j.1365-2559.2001.01082.x PMID: 11207825

48. Gouras GK, Tsai J, Naslund J, Vincent B, Edgar M, Checler F, et al. Intraneuronal Aβ42 accumulation in human brain. Am J Pathol. 2000; 156:15–20. https://doi.org/10.1016/S0002-9440(10)64700-1 PMID: 10623648

49. Collins-Praino LE, Francis YI, Griffith EY, Wiegman AF, Urbach J, Lawton A, et al. Soluble amyloid beta levels are elevated in the white matter of Alzheimer's patients, independent of cortical plaque severity. Acta Neuropathol Commun. 2014; 2:1–10. https://doi.org/10.1186/s40478-014-0083-0 PMID: 25129614

50. Lazarov O, Lee M, Peterson DA, Sisodia SS. Evidence that synaptically released β-amyloid accumulates as extracellular deposits in the hippocampus of transgenic mice. J Neurosci. 2002; 22:9785–9793. https://doi.org/10.1523/jneurosci.22-22-09785.2002 PMID: 12427834

51. Cirrito JR, Yamada KA, Finn MB, Sloviter RS, Bales KR, May PC, et al. Synaptic activity regulates interstitial fluid amyloid-β levels in vivo. Neuron. 2005; 48:913–922. https://doi.org/10.1016/j.neuron.2005.10.028 PMID: 16364896

52. Harris SS, Wolf F, De Strooper B, Busche MA. Tipping the Scales: Peptide-Dependent Dysregulation of Neural Circuit Dynamics in Alzheimer's Disease. Neuron. 2020; 107:417–435. https://doi.org/10.1016/j.neuron.2020.06.005 PMID: 32579881

53. Self WK, Holtzman DM. Emerging diagnostics and therapeutics for Alzheimer disease. Nat Med. 2023. https://doi.org/10.1038/s41591-023-02505-2 PMID: 37667136

54. Zhu K, Xiang X, Filser S, Marinković P, Dorostkar MM, Crux S, et al. Beta-Site Amyloid Precursor Protein Cleaving Enzyme 1 Inhibition Impairs Synaptic Plasticity via Seizure Protein 6. Biol Psychiatry. 2018; 83:428–437. https://doi.org/10.1016/j.biopsych.2016.12.023 PMID: 28129943

55. Francis JS, Markov V, Wojtas ID, Gray S, McCown T, Samulski RJ, et al. Preclinical biodistribution, tropism, and efficacy of oligotropic AAV/Olig001 in a mouse model of congenital white matter disease. Mol Ther - Methods Clin Dev. 2021; 20:520–534. https://doi.org/10.1016/j.omtm.2021.01.009 PMID: 33614826

56. Pachitariu M, Sridhar S, Stringer C. Solving the spike sorting problem with Kilosort. bioRxiv. 2023. https://doi.org/10.1101/2023.01.07.523036

57. McNamara CG, Tejero-Cantero Á, Trouche S, Campo-Urriza N, Dupret D. Dopaminergic neurons promote hippocampal reactivation and spatial memory persistence. Nat Neurosci. 2014; 17:1658–1660. https://doi.org/10.1038/nn.3843 PMID: 25326690

58. Holt GR, Softky WR, Koch C, Douglas RJ. Comparison of discharge variability in vitro and in vivo in cat visual cortex neurons. J Neurophysiol. 1996; 75:1806–1814. https://doi.org/10.1152/jn.1996.75.5.1806 PMID: 8734581

59. Gava GP, McHugh SB, Lefèvre L, Lopes-dos-Santos V, Trouche S, El-Gaby M, et al. Integrating new memories into the hippocampal network activity space. Nat Neurosci. 2021; 24:326–330. https://doi.org/10.1038/s41593-021-00804-w PMID: 33603228

60. Nitzan N, Swanson R, Schmitz D, Buzsáki G. Brain-wide interactions during hippocampal sharp wave ripples. Proc Natl Acad Sci U S A. 2022;119. https://doi.org/10.1073/pnas.2200931119 PMID: 35561219

61. Nitzan N, McKenzie S, Beed P, English DF, Oldani S, Tukker JJ, et al. Propagation of hippocampal ripples to the neocortex by way of a subiculum-retrosplenial pathway. Nat Commun. 2020;11. https://doi.org/10.1038/s41467-020-15787-8 PMID: 32327634

62. Reinhardt P, Glatza M, Hemmer K, Tsytsyura Y, Thiel CS, Höing S, et al. Derivation and Expansion Using Only Small Molecules of Human Neural Progenitors for Neurodegenerative Disease Modeling. PLoS ONE. 2013;8. https://doi.org/10.1371/journal.pone.0059252 PMID: 23533608

63. Hall CE, Yao Z, Choi M, Tyzack GE, Serio A, Luisier R, et al. Progressive Motor Neuron Pathology and the Role of Astrocytes in a Human Stem Cell Model of VCP-Related ALS. Cell Rep. 2017; 19:1739–1749. https://doi.org/10.1016/j.celrep.2017.05.024 PMID: 28564594

64. Garcia-Reitboeck P, Phillips A, Piers TM, Villegas-Llerena C, Butler M, Mallach A, et al. Human Induced Pluripotent Stem Cell-Derived Microglia-Like Cells Harboring TREM2 Missense Mutations Show Specific Deficits in Phagocytosis. Cell Rep. 2018; 24:2300–2311. https://doi.org/10.1016/j.celrep.2018.07.094 PMID: 30157425

65. Xiang X, Piers TM, Wefers B, Zhu K, Mallach A, Brunner B, et al. The Trem2 R47H Alzheimer's risk variant impairs splicing and reduces Trem2 mRNA and protein in mice but not in humans. Mol Neurodegener. 2018; 13:1–14. https://doi.org/10.1186/s13024-018-0280-6 PMID: 30185230

66. Baghallab I, Reyes-Ruiz JM, Abulnaja K, Huwait E, Glabe C. Epitomic Characterization of the Specificity of the Anti-Amyloid Aβ Monoclonal Antibodies 6E10 and 4G8. J Alzheimers Dis. 2018; 66:1235–1244. https://doi.org/10.3233/JAD-180582 PMID: 30412489

67. Emin D, Zhang YP, Lobanova E, Miller A, Li X, Xia Z, et al. Small soluble α-synuclein aggregates are the toxic species in Parkinson's disease. Nat Commun. 2022; 13:1–15. https://doi.org/10.1038/s41467-022-33252-6 PMID: 36127374

68. Strauss S, Jungmann R. Up to 100-fold speed-up and multiplexing in optimized DNA-PAINT. Nat Methods. 2020; 17:789–791. https://doi.org/10.1038/s41592-020-0869-x PMID: 32601424

69. Danial JSH, Garcia-Saez AJ. Quantitative analysis of super-resolved structures using ASAP. Nat Methods. 2019; 16:711–714. https://doi.org/10.1038/s41592-019-0472-1 PMID: 31263253

70. Srinivasan K, Friedman BA, Etxeberria A, Huntley MA, van der Brug MP, Foreman O, et al. Alzheimer's Patient Microglia Exhibit Enhanced Aging and Unique Transcriptional Activation. Cell Rep. 2020; 31:107843. https://doi.org/10.1016/j.celrep.2020.107843 PMID: 32610143

71. Vasistha NA, Johnstone M, Barton SK, Mayerl SE, Thangaraj Selvaraj B, Thomson PA, et al. Familial t(1;11) translocation is associated with disruption of white matter structural integrity and oligodendrocyte–myelin dysfunction. Mol Psychiatry. 2019;1641–1654. https://doi.org/10.1038/s41380-019-0505-2 PMID: 31481758

72. Swire M, Kotelevtsev Y, Webb DJ, Lyons DA, Ffrench-Constant C. Endothelin signalling mediates experience-dependent myelination in the CNS. Elife. 2019; 8:1–23. https://doi.org/10.7554/eLife.49493 PMID: 31657718

73. Bourdenx M, Martín-Segura A, Scrivo A, Rodriguez-Navarro JA, Kaushik S, Tasset I, et al. Chaperone-mediated autophagy prevents collapse of the neuronal metastable proteome. Cell. 2021; 184:2696–2714.e25. https://doi.org/10.1016/j.cell.2021.03.048 PMID: 33891876

74. Klionsky DJ, Abdel-Aziz AK, Abdelfatah S, Abdellatif M, Abdoli A, Abel S, et al. Guidelines for the use and interpretation of assays for monitoring autophagy (4th edition)1. Autophagy. 2021; 17:1–382. https://doi.org/10.1080/15548627.2020.1797280 PMID: 33634751

75. Shi Y, Kirwan P, Smith J, Robinson HPC, Livesey FJ. Human cerebral cortex development from pluripotent stem cells to functional excitatory synapses. Nat Neurosci. 2012; 15:477–486. https://doi.org/10.1038/nn.3041 PMID: 22306606